

Effect of ICME-Driven Storms on Field-Aligned and Ionospheric Currents From AMPERE and SuperMAG

M. N. Pedersen¹ , H. Vanhamäki¹ , A. T. Aikio¹ , C. L. Waters² , J. W. Gjerloev^{3,4} , S. Käki^{5,6} , and A. B. Workayehu¹ 

¹Space Physics and Astronomy Research Unit, University of Oulu, Oulu, Finland, ²School of Mathematical and Physical Sciences, University of Newcastle, Callaghan, NSW, Australia, ³The Johns Hopkins University Applied Physics Laboratory, Laurel, MD, USA, ⁴Faculty for Physics and Technology, University of Bergen, Bergen, Norway, ⁵Finnish Meteorological Institute, Helsinki, Finland, ⁶Division of Particle Physics and Astrophysics, University of Helsinki, Helsinki, Finland

Key Points:

- High p_{dyn} storms are mainly driven by sheath regions ahead of the interplanetary coronal mass ejection (ICME) ejecta and low p_{dyn} storms are mainly driven by magnetic clouds (MC)
- Sheath (high p_{dyn}) storms have field-aligned current (FAC) that peak 1 hr after t_0 , while MC (low p_{dyn}) storms develop gradually and have FAC that peak 11 hr after t_0
- Russell-McPherron effect is less frequently observed in ICME storms (44%) than in high speed streams/stream interaction regions storms (82%)

Supporting Information:

Supporting Information may be found in the online version of this article.

Correspondence to:

M. N. Pedersen,
marcus.pedersen@oulu.fi

Citation:

Pedersen, M. N., Vanhamäki, H., Aikio, A. T., Waters, C. L., Gjerloev, J. W., Käki, S., & Workayehu, A. B. (2022). Effect of ICME-driven storms on field-aligned and ionospheric currents from AMPERE and SuperMAG. *Journal of Geophysical Research: Space Physics*, 127, e2022JA030423. <https://doi.org/10.1029/2022JA030423>

Received 25 FEB 2022
Accepted 26 JUL 2022

Abstract This study investigates the field-aligned currents (FACs) and ionospheric equivalent currents for interplanetary coronal mass ejection (ICME)-driven storms by considering 45 events with a minimum $\text{Dst} \leq -50$ nT. The FACs and ionospheric equivalent currents are studied by applying a superposed epoch analysis to data from AMPERE and SuperMAG with the zero epoch (t_0) centered at the onset of the storm main phase. The currents and number of substorm onsets begin to increase 3 hr before t_0 and maximizes about 1 hr after t_0 . The currents and number of substorm onsets remain high throughout the entire storm main phase, until at $t_0 + 14$ hr they start to slowly relax back to quiet time conditions. The storms were separated into two groups based on the solar wind dynamic pressure p_{dyn} around t_0 . High p_{dyn} storms are mostly driven by the sheath region ahead of the ejecta. These storms have short main phase durations and larger currents early in the main phase which maximize at $t_0 + 50$ min. The low p_{dyn} group contains storms that start during the magnetic clouds (MC) and have gradually increasing currents that maximize at $t_0 + 11$ hr, close to the end of the storm main phase. For the first 4 hr of the storm main phase, the currents in sheath-driven storms are larger than for MC-driven storms. The Russell-McPherron effect is less important for ICME-driven storms where only 44% have a contribution, compared to 82% of high speed stream/stream interaction driven storms.

Plain Language Summary Geomagnetic storms are responsible for the largest magnetospheric and ionospheric disturbances and can last up to several days. During storms, field-aligned currents (FACs) that couple the magnetosphere and the ionosphere intensify, increasing in magnitude by millions of ampere and are connected to large enhancements in the horizontally flowing ionospheric currents. In this study, the FACs and ionospheric currents have been studied statistically using data from 45 interplanetary coronal mass ejection (ICME) driven storms. It is found that the currents peak about 1 hr after the storm main phase onset and remain strongly intensified for the next 14 hr, before slowly decreasing back to normal time conditions. It is also shown that the solar wind dynamic pressure can to a large extent separate storms driven by the sheath region versus magnetic cloud (MC) region of the ICME. Sheath-driven storms have an abrupt increase in the currents shortly after the storm main phase onset, while MC-driven storms have gradual increase in currents that reach maximum 11 hr after onset. Sheath-driven storms drive larger currents than MC-driven storms for the first 4 hr after main phase onset. Afterward, the currents become larger for MC than sheath-driven storms.

1. Introduction

Geomagnetic storms were defined by Gonzalez et al. (1994) as an interval of time when a sufficiently intense and long-lasting interplanetary convection electric field leads, through a substantial energization in the magnetosphere-ionosphere system, to an intensified ring current strong enough to exceed some key threshold of the quantifying storm time Dst index. The majority of geomagnetic storms are caused by interplanetary coronal mass ejections (ICMEs) or high speed streams (HSSs) and associated solar wind stream interaction regions/corotating interaction regions (SIRs/CIRs) (e.g., Kamide et al., 1998). ICMEs have been shown to be responsible for storms with characteristics such as storm sudden commencement (SSC), the most intense events measured by Dst depression, saturation of the cross-polar cap potential and largest geomagnetically induced currents (GIC) (e.g., Borovsky & Denton, 2006). In contrast, HSS/SIR driven storms usually have a gradual development in the Dst, longer lasting impact on geospace and longer magnetospheric convection intervals (see e.g., Borovsky & Denton, 2006; Burns et al., 2012; Turner et al., 2009).

© 2022. The Authors.

This is an open access article under the terms of the [Creative Commons Attribution License](https://creativecommons.org/licenses/by/4.0/), which permits use, distribution and reproduction in any medium, provided the original work is properly cited.

ICMEs are the interplanetary counterpart of CMEs observed at the Sun, where gigantic magnetized plasma clouds are launched into interplanetary space (e.g., Kilpua et al., 2017). When the ICME main ejecta propagates through interplanetary space faster than the ambient solar wind, a sheath region is created (Yermolaev et al., 2021). Sheath regions ahead of the ICME main ejecta are often turbulent and characterized by large variability in the solar wind (SW) and interplanetary magnetic field (IMF) with high proton temperature and density (e.g., Kilpua et al., 2017; Siscoe & Odstrcil, 2008). The mean duration of a sheath region at Earth orbit reported by Kilpua et al. (2017) was 11.1 hr, corresponding to a mean width of ~ 0.13 AU.

Some of the ICME main ejecta can be characterized as magnetic clouds (MCs). MCs are the interplanetary manifestation of coronal mass ejection magnetic flux ropes and have an average size of 0.25 AU at Earth orbit (Burlaga et al., 1982; Vourlidas et al., 2013). MCs have enhanced IMF magnitudes compared with the ambient solar wind and are characterized by a smooth rotation of the magnetic field direction over 180° (Burlaga et al., 1981, 1982; Klein & Burlaga, 1982). The total pressure inside MCs at 1 AU is 2–3 times higher than outside the cloud, and therefore the MC expands outward, with an average velocity of half the Alfvén speed at 1 AU (Burlaga et al., 1982). Due to the expansion of the MC, the proton temperature inside the MC is smaller than the predicted value based on the typical relationship between proton temperature and solar wind velocity (Gosling et al., 1973). The difference between the observed and expected proton temperature has been one of the key detection parameters used in the well-known ICME list by Richardson and Cane (2010). Only about one-third of ICMEs detected at 1 AU show clear signatures of MCs. However, it is believed that a larger fraction of ICMEs contain MC structures or flux ropes, but that they are not always detected as the satellites do not always pass through the center of the MC (Kilpua et al., 2017). Cane and Richardson (2003) report that the majority of ICMEs occurring during solar minimum have observable MCs, while this decreases to less than 20% for ICMEs during solar maximum.

Yermolaev et al. (2012) reported that the geoeffectiveness in terms of probability of generating a geomagnetic storm, is higher for MCs than sheaths and CIRs. According to Kilpua et al. (2017) sheaths are the most geoeffective structure in the ascending phase and near solar maximum. The geoefficiency, in accordance with “output/input” criteria, has been reported to be higher for sheath than MC-driven storms (Turner et al., 2009; Yermolaev et al., 2010, 2012) and higher during high solar wind density conditions compared to low density conditions (Nakano & Kataoka, 2022). Pulkkinen et al. (2007) reported a superposed epoch analysis (SEA) showing the differences in the solar wind driver and magnetospheric responses between sheath and MC-driven storms. They reported that the magnetosphere responded slower to MC storms than to sheath storms, and that both groups had similar SYM-H minima although the driving during MC storms was weaker.

Southward IMF B_z is an important factor determining geomagnetic storm intensity, both for CIR and ICME driven storms (Hutchinson et al., 2011). The probability for southward IMF B_z to occur changes with the varying angle between the Y axis in the solar equatorial coordinate system (where solar wind is ordered), and the Z axis in the solar magnetospheric coordinate system (where the SW-magnetosphere coupling is ordered). This gives rise to a semiannual variation in geomagnetic activity known as the Russell-McPherron (RM) effect (Russell & McPherron, 1973). The RM effect influences the occurrence of storms, their duration and their strength (e.g., Russell & McPherron, 1973; Zhao & Zong, 2012). Alves et al. (2006) showed that 33% of all CIRs were geoeffective, but during equinoxes this rose to 50%, which they attributed to the RM effect. Pedersen et al. (2021) reported that 82% of HSS/SIR storms had contribution from the RM effect, and that both low and high p_{dyn} HSS/SIR storms were equally influenced by the RM effect.

The enhanced energy input to the magnetosphere during geomagnetic storms is manifested by increased field-aligned currents (FACs), also known as Birkeland currents, which are connected to ionospheric currents. During geomagnetic storms, several substorms typically take place. The FACs and ionospheric currents are particularly enhanced during substorms, hence a large part of research has focused on the evolution of these current systems during magnetospheric substorms (e.g., Clausen et al., 2013; Coxon et al., 2014; Forsyth et al., 2018; Iijima & Potemra, 1978; Käki et al., 2022; McPherron et al., 2018). Substorms are categorized into three phases, the growth phase (~ 60 min), the expansion phase (~ 20 min) and a recovery phase (~ 2.5 hr) (e.g., McPherron, 1979; McPherron et al., 2018). During the substorm growth phase, region 1 FACs on the dayside become stronger than nightside and start to move equatorward as open magnetic flux is added to the polar cap (Clausen et al., 2013). Both the region 1 (R1) and region 2 (R2) currents and the horizontal ionospheric currents slowly increase during the substorm growth phase, with a rapid increase starting at substorm onset and maximize during the substorm expansion phase before returning to their initial levels (Coxon et al., 2014).

The evolution of the ionospheric current and FACs during geomagnetic storms is less understood. In 2009 the Active Magnetosphere and Planetary Electrodynamics Response Experiment (AMPERE) using the Iridium constellation satellites started providing global coverage of the FACs at high spatial and temporal resolution (Anderson et al., 2000, 2002; Waters et al., 2001, 2020). Since the introduction of AMPERE, there have been several case studies of the FACs during geomagnetic storms (e.g., Knipp et al., 2014; Le et al., 2016; Lyons et al., 2016; Wilder et al., 2012). Le et al. (2016) reported that after a prolonged period of strongly southward IMF, AMPERE observed significant intensification of FACs, and that during the large storm the FACs moved equatorward as low as $\sim 60^\circ$ magnetic latitude (MLAT). In a few events, Feldstein et al. (1997) found that the eastward and westward equivalent currents was of equal strength during the storm initial phase, while the westward dominates and sometimes show signatures of saturation during the storm main phase. One of the challenges of capturing the evolution of the currents during storms is that the sequence of substorms is not the same from storm to storm. Still, geomagnetic storms are responsible for some of the largest currents that are known to cause GICs. Therefore, a good understanding of the FACs and ionospheric currents on timescales of storms is important for mitigating hazardous space weather events.

Because of the transition to the second generation of Iridium satellites, AMPERE provides data products up to September 2017 as of the time of writing. SuperMAG provides high spatial and temporal resolution magnetometer data that can be used to resolve the ionospheric equivalent currents (Gjerloev, 2009, 2012; Waters et al., 2015). With almost a full solar cycle of coincident SuperMAG and AMPERE data, a statistical SEA study can be used to investigate the temporal and spatial evolution of the ionospheric and FACs during geomagnetic storms produced by different interplanetary drivers. Pedersen et al. (2021), hereafter Paper 1, investigated the statistical evolution of the FACs and ionospheric equivalent currents during HSS/SIR geomagnetic storms. In Paper 1, the storms were divided into low and high dynamic pressure categories based on the maximum solar wind dynamic pressure near the storm onset time.

This paper describes the impact of ICME driven geomagnetic storms on the ionospheric and field-aligned current systems by utilizing AMPERE and SuperMAG data during the same time period as in Paper 1. This paper is organized as follows: Section 2 describes the event selection and data analysis method. In Section 3.1 the data analysis is applied to all storms together. Section 3.2 discusses the solar wind and storm properties for sheath and MC storms and shows the connection between high dynamic pressure near storm onset time to sheath-driven storms and low dynamic pressure to MC-driven storms. In Section 3.3 the FACs and ionospheric equivalent currents for sheath and MC-driven storms are presented and compared. Section 4 discusses the results and investigates the Russell-McPherron effect, solar wind coupling, ICME drivers, and compares the results to Paper 1 for HSS/SIR driven storms. Section 5 contains the conclusions.

2. Data, Event Selection, and Analysis Method

2.1. Data

The same northern hemisphere data sources and superposed epoch analysis technique were used in this study as in Paper 1. AMPERE provides the FAC densities at 2 min cadence over a 10 min window with spatial resolution of 1° MLAT and 1 hr magnetic local time (MLT) (Anderson et al., 2000, 2002; Waters et al., 2001, 2020). SuperMAG provides gridded ground magnetometer perturbations and the substorm onset list (Gjerloev, 2009, 2012; Waters et al., 2015; Newell & Gjerloev, 2011a, 2011b). The ground magnetometer perturbations have a temporal resolution of 1 min and spatial resolution of 2° MLAT and 1 hr MLT. OMNIWeb provides the solar wind plasma and IMF parameters delayed to the bowshock, as well as the AE, AL, AU, SYM-H, and Dst indices (King & Papitashvili, 2005). All OMNIWeb IMF/SW data used have 5 min temporal resolution. All indices have 1 min temporal resolution except for the Dst index which has 1 hr resolution.

2.2. Selecting ICME-Driven Geomagnetic Storms

To select moderate geomagnetic storms, an algorithm was applied to the Dst index, searching for events that reached a disturbance of at least -50 nT. The -50 nT limit is commonly used as the threshold between weak and moderate storms (see e.g., Gonzalez et al., 1994; Loewe & Pröls, 1997). The same algorithm was used in Paper 1, and in that study the storm main phase onset was set to the hour the Dst index decreased to less than -15 nT. The SYM-H index, which is a 1 min time resolution index designed to measure the intensity of the storm time

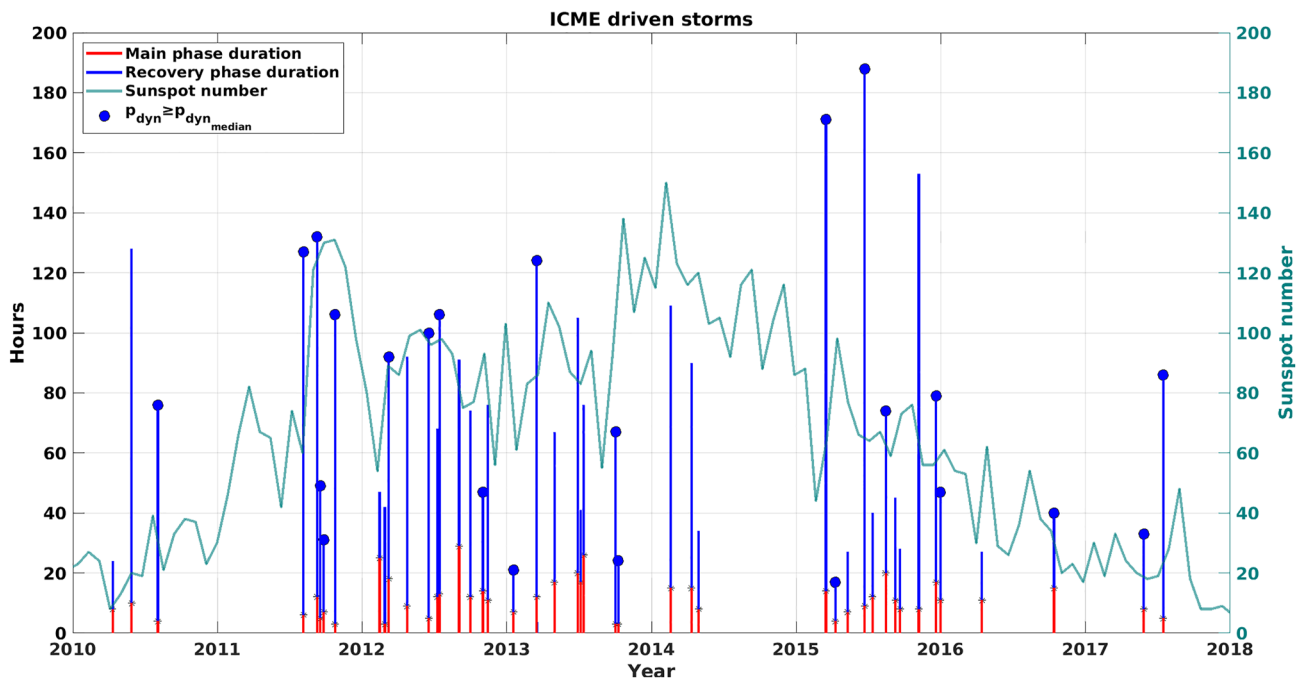


Figure 1. Distribution of the 45 interplanetary coronal mass ejection (ICME) driven storms in Table 1. The red (blue) line shows the duration of the main (recovery) phase. The events with a solid circle at the top are among the high dynamic pressure group.

ring current, has shown excellent comparison to the 1 hr Dst index (Wanliss & Showalter, 2006). In this study, the onset time found with the algorithm was fine-tuned to the time the 10-min averaged SYM-H index decreased to less than -15 nT. This gives improved accuracy in the storm main phase onset time, which is used in the superposed epoch analysis. The end time of the storm was set as the time when the Dst index (after reaching a minimum ≤ -50 nT) increased above -15 nT. All storms found using this algorithm were then compared to the ICME list by Richardson and Cane (2010) (<http://www.srl.caltech.edu/ACE/ASC/DATA/level3/icmetable2.htm>), and only storms that have main phase onset during an ICME event were categorized as ICME driven storms.

In total 58 ICME storms were detected between the years 2010 and 2017, but only 45 of these had full AMPERE data coverage. These 45 storms are the events in this study, and are summarized in Table 1 and Figure 1. The majority of the events occurred during August 2011 to April 2014 (26 storms) at the maximum period of the solar cycle, and in the year 2015 (11 storms), at the beginning of the declining phase of the solar cycle. In Paper 1, the HSS/SIR storms occurred mostly during the declining phase, which is consistent with previous studies (e.g., Borovsky & Denton, 2006; Grandin et al., 2019; Richardson et al., 2001). Seventeen of the 45 storms have $Dst < -100$ nT, which puts 38% of the storms in the large storm category. Table 1 and Figure 1 also show the dynamic pressure group of the storms, which will be discussed further in Section 3.2. The “Sh/MC onset” column indicates if the storm is in the sheath (sh) region or the magnetic cloud (MC) region at the time of zero epoch (t_0) based on visual inspection of the solar wind data for each event. Column 5 in Table 1 shows the IMF sector polarity, indicating whether the storm had a contribution from the RM effect following the “spring-toward fall-away” rule (Miyoshi & Kataoka, 2008). Events with S-T and F-A had a contribution from the RM effect, the others did not. Columns 6, 7, and 8 show the main phase duration, recovery phase duration and the Dst minimum, respectively.

2.3. Data Analysis

The storms were studied by using the superposed epoch analysis (SEA) technique with zero epoch (t_0) at the time of storm main phase onset (when the 10-min averaged SYM-H index decreased below -15 nT as explained in Section 2.2). The choice of t_0 is important, and must be chosen according to the phenomena of interest (Ilie et al., 2008). Setting t_0 to the main phase onset allows the study of the temporal and spatial development of the currents as the storm evolves, and to relate the currents to the driving solar wind parameters. Another option

Table 1
Table of the 45 ICME Events Included in This Study

Storm number	Main phase onset (zero epoch)	Low/High p_{dyn}	Sh/MC onset	Spring/Fall Toward/Away	Main phase (hr)	Recovery phase (hr)	Dst min (nT)
1	11-Apr-2010 16:50	Low	Sh ^{10hr} MC ↑	S-T	8	16	-67
2	29-May-2010 02:00	Low	MC		10	118	-80
3	03-Aug-2010 21:10	High	Sh ^{13hr} MC ↓	F-T	4	72	-74
4	05-Aug-2011 22:30	High	Sh	F-T	6	121	-115
5	09-Sep-2011 16:00	High	Sh ^{13hr} MC ↑	F-T	12	120	-75
6	17-Sep-2011 10:00	High	Sh ^{6hr} MC ↓↑	F-A	5	44	-72
7	26-Sep-2011 16:00	High	Sh	F-A	7	24	-118
8	24-Oct-2011 22:40	High	Sh ^{3hr} MC ↑	F-A	3	103	-147
9	14-Feb-2012 15:10	Low	Sh ^{10hr} MC ↓	S-T	25	22	-67
10	27-Feb-2012 15:20	Low	Sh ^{3hr} MC ↑	S-A	3	39	-57
11	08-Mar-2012 14:50	High	Sh ^{14hr} MC ↓	S-A	18	74	-145
12	23-Apr-2012 19:20	Low	MC	S-T	9	83	-120
13	17-Jun-2012 09:10	High	MC		5	95	-86
14	09-Jul-2012 00:50	Low	Sh/MC		12	56	-78
15	15-Jul-2012 03:40	High	Sh ^{4hr} MC ↓		13	93	-139
16	02-Sep-2012 03:30	Low	MC	F-A	29	62	-69
17	30-Sep-2012 14:50	Low	Sh ^{7hr} MC ↓↑	F-A	12	62	-122
18	01-Nov-2012 06:20	High	MC	F-T	14	33	-65
19	13-Nov-2012 19:20	Low	MC	F-A	11	65	-108
20	17-Jan-2013 15:30	High	Sh ^{1hr} MC ↓↑		7	14	-52
21	17-Mar-2013 07:50	High	Sh ^{8hr} MC ↓↑	S-T	12	112	-132
22	01-May-2013 02:10	Low	MC	S-T	17	50	-72
23	28-Jun-2013 10:40	Low	MC		20	85	-102
24	06-Jul-2013 01:40	Low	MC		17	24	-87
25	13-Jul-2013 19:50	Low	MC		26	50	-81
26	02-Oct-2013 04:30	High	Sh ^{20hr} MC ↑	F-T	3	64	-72
27	08-Oct-2013 22:20	High	Sh	F-A	3	21	-69
28	18-Feb-2014 17:10	Low	MC	S-A	15	94	-119
29	11-Apr-2014 19:20	Low	MC	S-T	15	75	-87
30	30-Apr-2014 00:40	Low	MC	S-A	8	26	-67
31	17-Mar-2015 07:30	High	Sh ^{7hr} MC ↓	S-T	14	157	-223
32	10-Apr-2015 00:20	High	Sh ^{14hr} MC ↓	S-A	4	13	-75
33	10-May-2015 21:30	Low	MC	S-A	7	20	-76
34	22-Jun-2015 19:20	High	Sh		9	179	-204
35	13-Jul-2015 03:00	Low	Sh ^{14hr} MC ↓↑		12	28	-61
36	15-Aug-2015 11:10	High	Sh	F-A	20	54	-84
37	09-Sep-2015 00:50	Low	MC	F-A	11	34	-98
38	20-Sep-2015 06:40	Low	Sh	F-A	8	20	-75
39	06-Nov-2015 21:50	Low	Sh ^{12hr} MC ↓↑	F-A	8	145	-89
40	20-Dec-2015 05:40	High	Sh ^{12hr} MC ↓		17	62	-155
41	31-Dec-2015 13:00	High	Sh ^{6hr} MC ↓		11	36	-110
42	14-Apr-2016 09:30	Low	Sh/MC	S-T	11	16	-59
43	13-Oct-2016 07:10	High	MC ^{-2hr} Sh	F-A	15	25	-104

Table 1
Continued

Storm number	Main phase onset (zero epoch)	Low/High p_{dyn}	Sh/MC onset	Spring/Fall Toward/Away	Main phase (hr)	Recovery phase (hr)	Dst min (nT)
44	27-May-2017 23:10	High	MC ^{-1hr} Sh		8	25	-125
45	16-Jul-2017 10:50	High	Sh ^{10hr} MC		5	81	-72

Note. The “Sh/MC onset” in column 4 indicates if the ICME is in the sheath (Sh) or magnetic cloud (MC) region at the time of t_0 . The number following Sh (MC) is the time until (after) the MC (sheath) is encountered (if there are any), and the arrow indicates if the MC has southward or northward B_z . If there are two arrows then the MC changes B_z direction during the cloud, and the first (last) arrow shows how it starts (ends). For storms starting with MC there are no arrows since all have southward B_z at t_0 .

would be to use the “double” or “triple” SEA (Lepping et al., 2003; Yermolaev et al., 2010; Yokoyama & Kamide, 1997), where two or three reference points are used and the duration is re-scaled for each storm so the reference points coincide. However, here we use a simple SEA with the main phase onset as the only reference time, because it organizes the rapid development of the currents early in the storm well, leaves the time axis in real time and is consistent with the earlier HSS/SIR storm study reported in Paper 1.

Hemispheric maps of the FAC and ionospheric equivalent currents were constructed by superposing the currents at each MLT/MLAT grid point, then displaying the median value at each time step as explained in Paper 1. The total FACs were spatially integrated over all MLT hours and MLAT $\geq 40^\circ$, and the equivalent currents (J_{eq}) were integrated between $56\text{--}74^\circ$ MLAT to focus on the auroral electrojets. The low-latitude limit was selected to avoid contributions from mid-latitude ionospheric/magnetospheric currents.

The solar wind dynamic pressure p_{dyn} and the Newell coupling function (NCF) (Newell et al., 2007) were calculated using the OMNI solar wind data. The solar wind dynamic pressure was calculated as:

$$p_{\text{dyn}} = m_p n_{\text{SW}} V_{\text{SW}}^2, \quad (1)$$

where m_p is the proton mass, n_{SW} is the solar wind electron density and V_{SW} is the solar wind flow velocity. The NCF is a measure of the rate at which magnetic flux at the magnetopause Φ_{MP} is opened (Newell et al., 2007) and is calculated as:

$$\frac{d\Phi_{\text{MP}}}{dt} = V_{\text{SW}}^{4/3} B_T^{2/3} \sin^{8/3}(\theta_c/2), \quad (2)$$

where B_T is the transverse component of the IMF magnitude ($B_T = \sqrt{B_Y^2 + B_Z^2}$) and θ_c is the IMF clock-angle.

3. Results

3.1. Superposed Epoch Analysis of All ICME Storms

Figure 2 shows the superposed IMF and SW parameters for all ICME-driven storms. Panel (a) shows the NCF with a rapid increase in SW-magnetospheric coupling beginning 4 hr before t_0 . The NCF shows two maxima around t_0 , first at $t_0 - 50$ min and a second at $t_0 + 1.5$ hr, before slowly decreasing back to quiet time conditions after about 1 day. Four hours before t_0 , the IMF magnitude starts increasing from 7 to 14 nT at t_0 . Slightly later, starting at $t_0 - 3$ hr the B_z component turns southward and minimizes at -7.9 nT 20 min before t_0 and remains strongly southward with values between -7.7 nT and -5.5 nT until $t_0 + 13$ hr. The influence of B_Y in panel (e) is suppressed as both storms with positive and negative B_Y are superposed. However, the variance in B_Y , as seen from the upper and lower quartiles, is largest between $t_0 - 3$ and $t_0 + 3$ hr, and decreases as the storm progresses. The median V_{SW} in panel (f) increases from 400 km/s to 440 km/s 3 hr before t_0 , with a more pronounced and longer-lasting increase seen in the upper quartile of V_{SW} . The solar wind flow velocity slightly decreases for the first 14 hr after t_0 before it continues to slowly increase throughout the remaining of the storm, reaching the largest values of 490 km/s at the end of the study window 2.5 days after t_0 . Panel (g) shows the proton temperature, T_p . An enhancement from $5.2 \cdot 10^4$ K to $7.9 \cdot 10^4$ K is seen in the median value 3 hr before t_0 at the time V_{SW} increases. The temperature then decreases during the first day after t_0 before reaching minimum of $2.7 \cdot 10^4$ K around $t_0 + 15$ hr. Meanwhile, the upper quartile shows large proton temperatures up to $3.2 \cdot 10^5$ K in the 3 hours

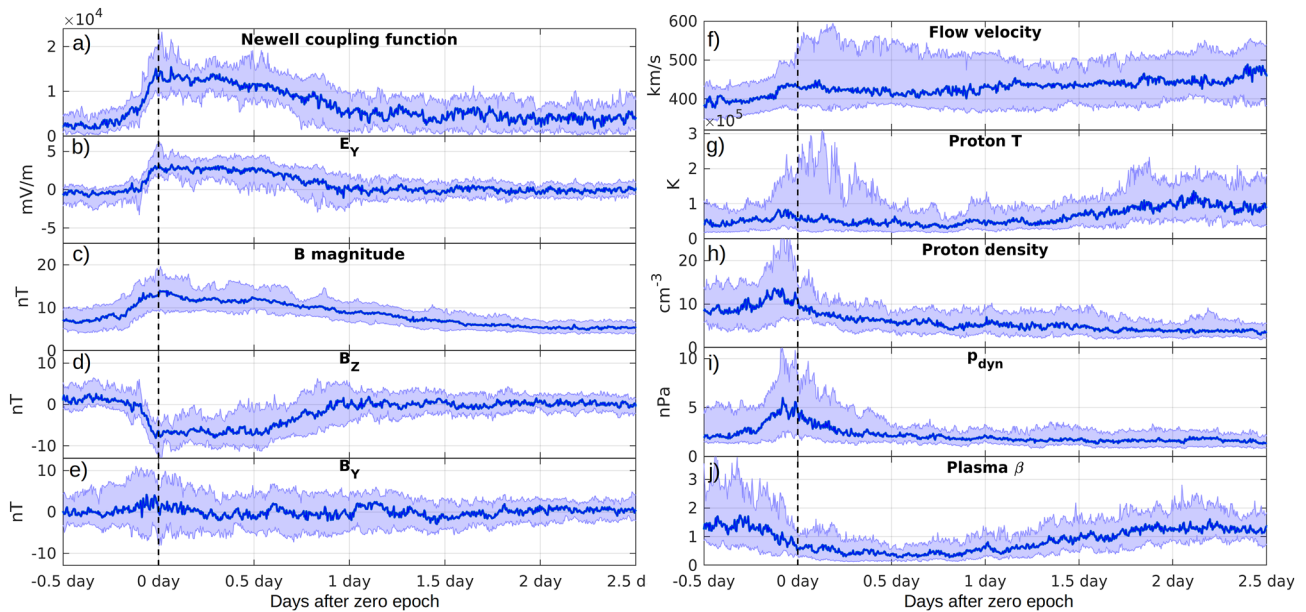


Figure 2. Superposed interplanetary magnetic field and solar wind parameters for all interplanetary coronal mass ejection events. The vertical dashed lines are the time of zero epoch (t_0), the solid lines show the median superposed values and the shaded areas enclose the upper and lower quartiles.

leading up to and after t_0 . Enhancements from 8 cm^{-3} to 14 cm^{-3} around t_0 are also seen in panel (h) for the proton density, but the maximum is reached before t_0 . After t_0 the proton density decreases throughout the storm and the variability seen in the upper and lower quartiles reduce. Panel (h) shows the plasma β parameter, where there is a clear decrease and long-lasting minimum of 0.3 during the first day of the storm, showing that the solar wind magnetic pressure generally exceeds the dynamic pressure during the first day after storm onset.

Many of the SW and IMF parameters in Figure 2 show signatures of the sheath and MC regions of ICMEs. The increase in V_{SW} 3 hr before t_0 may be a signature of the ICME propagating into the ambient solar wind, compressing and deflecting the plasma flow and creating a sheath region ahead of the ICME ejecta. This is associated with large enhancements in the upper quartile of the proton temperature T_p and density n_p around t_0 seen in panels (g) and (h). These enhancements are expected during the compressed sheath region following the forward shock. Meanwhile, the long lasting southward B_z , low proton temperature and low plasma β suggest the presence of MCs during the storm main phase. By checking the individual events, it is seen that the southward turnings of B_z before t_0 are associated either with the turbulent sheath regions, where the proton temperature and density are high and the magnetic field fluctuates strongly, or with the MC structure with low proton temperature and smooth magnetic field rotation. Thus Figure 2 shows solar wind and IMF signatures of both the sheath region and MC of an ICME. This is expected when superposing all storms with t_0 set to the geomagnetic storm main phase onset, as ICME driven storms are typically driven by either the sheath region or MC (e.g., Pulkkinen et al., 2007; Kilpua et al., 2017, and references therein). In the next section, storms are separated based on the maximum p_{dyn} around t_0 as was done in Paper 1, and it will be shown that this separation to a large extent distinguishes sheath-driven storms from MC-driven storms.

Figure 3 shows the superposed SYM-H index, AE, AU and AL indices, the integrated equivalent and downward field-aligned currents, and the average number of substorm onsets in one-hour bins for all ICME storms. Only the integrated downward FAC is shown as it is practically identical to the integrated upward FAC. The median and upper quartile of the SYM-H index in the top panel show some indication of SSC between 2–4 hr prior to t_0 , at the same time as the solar wind proton density starts increasing and reaches maximum. The superposed SYM-H minimum is -64 nT and is reached at $t_0 + 9.3 \text{ hr}$, but the SYM-H minimum is broad and the index stays small until $t_0 + 14 \text{ hr}$. The number of substorm onsets peaks near storm onset and again during SYM-H index minimum. The FAC and AE index begin to increase around the same time as the SSC is seen in the upper quartile, 3 hr before t_0 , and reach maximum 50 min after t_0 . The upward and downward FAC magnitudes are both between 7–8 MA throughout the main phase. The integrated westward J_{eq} has similar behavior as the integrated FAC, with a peak

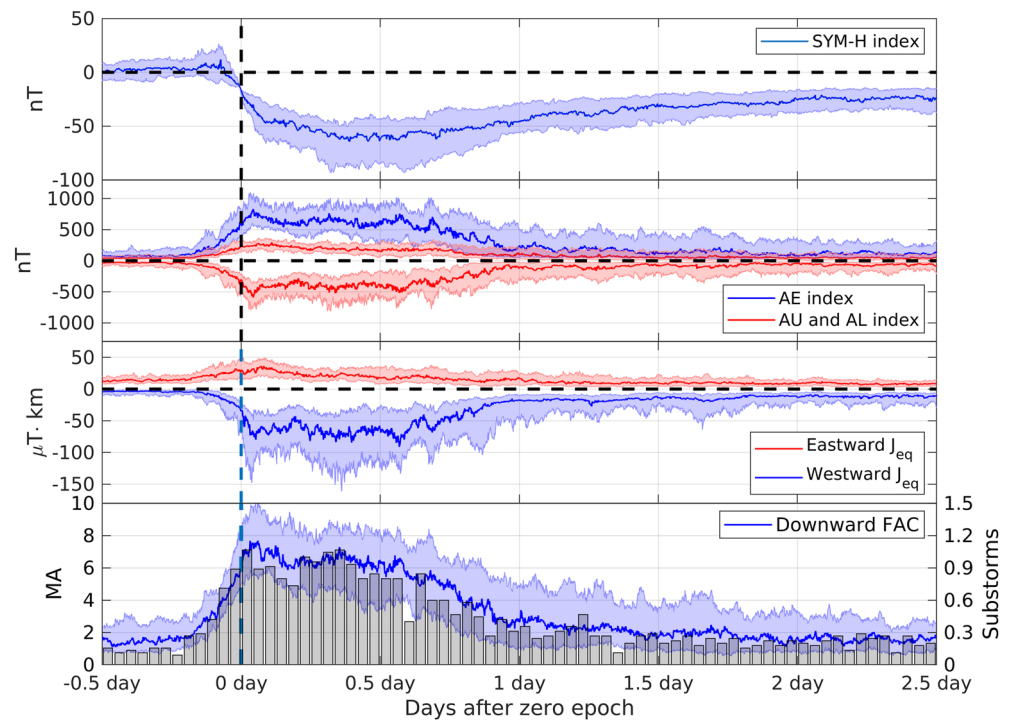


Figure 3. Top panel shows the superposed SYM-H index. The second panel is the superposed AE, AU and AL indices. The third panel shows the superposed integrated SuperMAG electrojets, J_{eq} . The bottom panel is the total integrated field-aligned current (FAC) with bars showing the average number of substorm onsets per storm occurring in 1-hr bins. The shaded areas show the upper and lower quartiles of the superposed values.

shortly after t_0 seen both in the median and lower quartile, but there are other intervals later during the SYM-H minimum of equal or larger values in both the median and quartiles. Meanwhile, the integrated eastward J_{eq} behaves differently than the integrated FAC and westward J_{eq} , and has only one peak at $t_0 + 60$ min. Following the peak, the integrated eastward J_{eq} starts decreasing throughout the remaining of the main phase.

3.2. Low and High Solar Wind Dynamic Pressure Versus Sheaths and MCs

In paper 1 the events were separated into two categories based on SW dynamic pressure around the main phase onset time [$t_0 - 3$ hr, $t_0 + 3$ hr]. Dynamic pressure can intensify solar wind-magnetospheric coupling at times of southward IMF and cause larger disturbances in the magnetosphere and ionosphere (e.g., Boudouridis et al., 2005; Palmroth et al., 2004). To investigate the impact of the dynamic pressure on ICME storms, the storms were separated into low and high p_{dyn} categories based on the maximum solar wind p_{dyn} within ± 3 hr around t_0 as described in Paper 1 for HSS/SIR storms. In Paper 1, the limiting p_{dyn} value was 6.8 nPa for HSS/SIR storms and in this study the limiting value is 6.1 nPa. In both cases, the value divide the events into two categories with about equal number of events. For the ICME events this gives 22 low p_{dyn} storms and 23 high p_{dyn} storms.

Figure 4a shows that during [$t_0 - 3$ hr, $t_0 + 3$ hr] the NCF, E_y , B , negative B_z , solar wind density, velocity, temperature and plasma β are larger in high p_{dyn} than low p_{dyn} events. For high p_{dyn} , several parameters including density and plasma β start increasing even before $t_0 - 3$ hr, and both density and p_{dyn} peak at 25 cm^{-3} and 11 nPa, respectively, at $t_0 - 3$ hr. The IMF B magnitude and negative B_z for high p_{dyn} events peak at t_0 with 17 nT and -12 nT, respectively, and solar wind velocity and temperature reach maxima of 550 km/s and $2.3 \cdot 10^5$ K at $t_0 + 3$ hr. During [$t_0 + 3$ hr, $t_0 + 1$ d] the magnitude of B and solar wind velocity remain larger for high p_{dyn} than low p_{dyn} storms, but negative B_z becomes smaller. In the first 12 hr after t_0 , solar wind density, p_{dyn} and temperature for high p_{dyn} events decrease to become similar in magnitude as for low p_{dyn} events.

High p_{dyn} events have clearly larger variability than low p_{dyn} events for most of the plasma parameters including B and B_z , which can be seen in the difference between the upper and lower quartiles (shaded colors). The low p_{dyn}

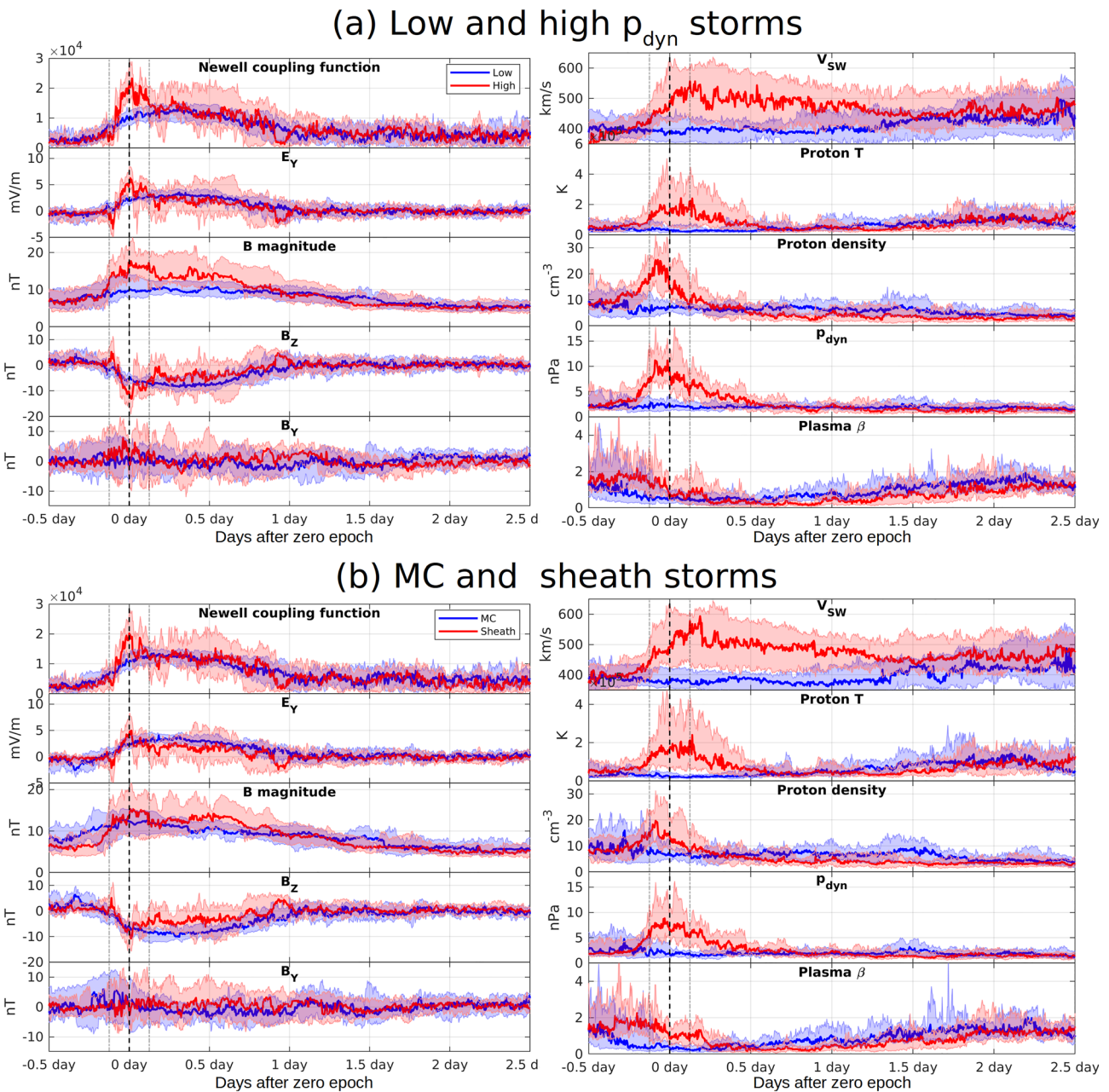


Figure 4. Superposed solar wind and interplanetary magnetic field parameters. (a) For the low and high pressure storms and (b) for the magnetic cloud (MC) and sheath-driven storms. The bold dashed vertical line shows the time of zero epoch, and the two faint dashed lines enclose the time interval that the dynamic pressure categories were selected.

events do not show similar enhancements around t_0 in the solar wind velocity, temperature and density as for high p_{dyn} events. Instead, the solar wind velocity remains steady around 400 km/s and the proton temperature remains low with values ranging from $1.8 \cdot 10^4$ K to $3.0 \cdot 10^4$ K between t_0 and $t_0 + 12$ hr, before starting to slightly increase toward the end of the storm. For the proton density some enhancement can be seen before $t_0 - 3$ hr. The IMF B magnitude and negative B_Z show a steady increase starting as early as $t_0 - 6$ hr that maximize 11 and 9 hr after t_0 with values of 11 nT and -9 nT, respectively.

The large proton temperature and density, as well as large fluctuations in the IMF strength and direction seen in the high p_{dyn} events are signatures of the sheath region preceding the main ejecta or MC (Kilpua et al., 2017). Also, the increase in V_{SW} is a signature of the forward shock that often develops between the ICME leading edge

and the ambient solar wind downstream. This indicates that high p_{dyn} storms are storms with onset during the sheath region of the ICME. Meanwhile, the low p_{dyn} storms have low proton temperature, proton density, plasma β and smooth variation in the IMF B_z component, which are all signatures of MC structures (Burlaga et al., 1981, 1982; Kilpua et al., 2017; Klein & Burlaga, 1982).

It turns out that the division based on a single parameter, p_{dyn} , near the storm main phase onset relatively well separates the storms into those which begin during the ICME sheath or MC regions, as discussed below. Table 1 column 4 was populated from visual inspection of several solar wind parameters of individual events and indicates for each storm whether it starts during the sheath region (26 events) or MC (19 events). MC regions were selected from the premise that they show signatures of smoothly rotating magnetic field structures and are usually accompanied by decreases in the proton temperature, large magnetic field values or low plasma β . ICMEs that propagate faster than the ambient solar wind creates a sheath region between the ambient solar wind and the ICME main ejecta. This region is characterized by an abrupt increase in solar wind velocity, large proton temperature and density and a strong fluctuating magnetic field. The MCs in Table 1 column 4 are in good agreement with Richardson and Cane (2010) (R&C) identification of MCs in their ICME list. Only two storms have a discrepancy with regard to MCs; in storm number 4 R&C detected a MC in the storm recovery phase that is not clear in our data, and in storm number 35 we identified a MC that was not reported by R&C. It should be noted that this study only considers OMNI solar wind and IMF data that is shifted to the Earth's bow shock nose, while R&C use data from multiple sources.

Fifteen of the 19 MCs storms (including the two “Sh/MC” storms with t_0 at the boundary between the sheath and the MC) are in the low p_{dyn} category. Of the remaining 4 MC storms that are in the high p_{dyn} category, two have t_0 very close to (≤ 2 hr) the sheath region, making these events p_{dyn} categorization influenced by the compressed plasma in the sheath region ahead of the MC. For the sheath-driven storms, 19 of 26 are in the high p_{dyn} category. This yields the low p_{dyn} category of $15/22 = 68\%$ MC-driven storms, while the high p_{dyn} category contains $19/23 = 82\%$ sheath-driven storms. Additionally, only 7 of the 26 storms with t_0 during the sheath region do not show signatures of a MC within the next 2.5 days following storm onset. In total 38 of 45, that is 86% of all ICMEs responsible for moderate-to-large storms in this study feature a MC. This fraction is larger than that of all ICMEs observed in interplanetary space, where only 1/3 contain an MC (Gosling, 1990; Jian et al., 2006).

For comparison, Figure 4b shows the superposed solar wind and IMF parameters for storms driven by the sheath (Sh) regions (26 storms) and MC regions (19 storms), following Table 1 column 4. Here, the similarities in the solar wind and IMF drivers between MC and low p_{dyn} as well as sheath and high p_{dyn} storms become clear. The NCF, E_y , B and B_z are slightly more abrupt at the onset of MC-driven storms than what is seen in (a) for low p_{dyn} storms, and median peak values in V_{SW} , proton density and p_{dyn} are slightly larger in the high p_{dyn} storms than sheath-driven storms.

Table 2 shows median values and median absolute deviations of selected parameters from individual events for the low and high p_{dyn} storms, as well as for sheath and MC-driven storms. The low p_{dyn} and MC storms have very similar values, likewise for the high p_{dyn} and sheath storms. The largest p_{dyn} values tend to occur during the compressed plasma in the sheath region ahead of the ICME ejecta (Gosling et al., 1978; Kilpua et al., 2017), and therefore high p_{dyn} around the time of t_0 effectively selects storms starting during the time the ICME sheath region interacts with the magnetopause.

Comparison between high and low p_{dyn} storms in Table 2 shows that the high p_{dyn} group has shorter main phase duration (8 vs. 12 hr) and largest storms measured by the Dst minimum (-104 nT vs. -79 nT). These values are consistent with earlier research showing that sheath-driven storms typically have shorter main phase durations and reach lower values of the Dst index compared to MC-driven storms (Pulkkinen et al., 2007; Yermolaev et al., 2007). Recovery phases are also longer for high than low p_{dyn} storms (64 vs. 50 hr), but the variability in the duration is large. This is consistent with Yermolaev et al. (2014) who showed that although there are large spreads in the recovery phase distributions, sheath-driven storms have longer recovery phase durations than MC storms. The time between the arrival of the ICME and t_0 was 15–16 hr for low p_{dyn} /MC storms and 4 hr for high p_{dyn} /sheath storms. This indicates that the high p_{dyn} /sheath-driven storms started typically a few hours after shock/sheath regions arrived at the magnetopause, while it took about 15 hr before the low p_{dyn} /MC-driven storms attained a Dst index of less than -15 nT.

Table 2
Properties of Low and High p_{dyn} , as Well as MC and Sheath-Driven Storms

	P_{dyn}		Region	
	Low	High	MC	Sheath
Number of storms	22	23	19	26
Median max p_{dyn}	3.6 ± 1.7 nPa	15 ± 2 nPa	4.5 ± 1.3 nPa	13 ± 4 nPa
Median min Dst	-79 ± 12 nT	-104 ± 32 nT	-86 ± 16 nT	-87 ± 27 nT
Min Dst in category	-122 nT	-223 nT	-125 nT	-223 nT
Median main phase duration	12 ± 3 hr	8.3 ± 4.2 hr	12 ± 3 hr	8.9 ± 4.4 hr
Median recovery phase duration	50 ± 25 hr	64 ± 39 hr	50 ± 25 hr	63 ± 37 hr
Median storm duration	67 ± 26 hr	76 ± 29 hr	68 ± 26 hr	76 ± 33 hr
Median time from ICME onset to t_0	15 ± 8 hr	3.8 ± 1.9 hr	16 ± 6 hr	3.5 ± 1.4 hr

Note. For the median values, the median absolute deviations are shown. The ICME onset time in the bottom row are from R&C <http://www.srl.caltech.edu/ACE/ASC/DATA/level3/icmetable2.htm> column (a).

When looking at individual storms in Table 1, all storms with Dst index < -130 nT are in the high p_{dyn} /sheath-driven group. In addition, none of the HSS/SIR storms in Paper 1 have Dst index < -130 nT, which shows that the largest storms during the time interval 2010–2017 are primarily driven by the sheath regions associated with ICME storms. The median main phase duration for low p_{dyn} /MC-driven storms is 12 hr. This is about half the duration of the median negative B_z in Figure 4 for low p_{dyn} /MC events.

3.3. Currents in Sheath and MC-Driven ICME Storms

For the purpose of physical interpretation of the ICME's influence on the evolution of the currents, the events have been separated by the interplanetary driver (sheath or MC), which is shown above to correspond well to high and low p_{dyn} ICME storms, respectively.

Figure 5 shows that the development of the SYM-H index is very different for the two interplanetary structures. Only the sheath storms show signatures of SSC before t_0 . They have a steeper decrease in the SYM-H index at the time of main phase onset, reach SYM-H minimum earlier and have a slower relaxation back to normal time condition in the recovery phase compared with MC storms. In earlier studies it has been shown that more than 75% of SSCs are driven by interplanetary shocks (e.g., Smith et al., 1986; Wang et al., 2006). The sheath storms have an abrupt increase in the AE index, integrated westward J_{eq} and FAC starting around $t_0 - 2$ hr, and reach respective maxima early in the storm main phase of 916 nT at $t_0 + 61$ min, $-114 \mu\text{T}\cdot\text{km}$ at $t_0 + 58$ min and 8.9 MA at $t_0 + 50$ min. On the other hand, MC storms have a gradual increase in the AE index, integrated westward J_{eq} and FAC starting around $t_0 - 4$ hr and reach respective maxima of 913 nT at $t_0 + 13.6$ hr, $-112 \mu\text{T}\cdot\text{km}$ at $t_0 + 11.4$ hr and 8.4 MA at $t_0 + 11.0$ hr. The temporal evolution of the integrated J_{eq} and FAC is similar to that of the NCF, as can be seen in Figure 4. The median difference between the upper and lower quartiles of the integrated FAC during the first day after t_0 is 4.4 MA for sheath storms and 2.7 MA for MC storms. This shows that the variability in the currents for sheath storms is substantially larger than for MC storms throughout the main phase of the storm. The number of substorm onsets have a large increase 2 hours before t_0 for the sheath storms, which is not seen for MC storms. For both sheath and MC-driven storms, number of substorm onsets peak at the same time as J_{eq} and FAC. In the late recovery phase, 2 days after t_0 , the number of substorm onsets, FAC, J_{eq} and AE index are all larger for the MC storms than the sheath storms.

To see how the currents evolve in different regions, the total integrated FAC is separated into four different MLT sectors: noon (9–15 MLT), dusk (15–21 MLT), midnight (21–03 MLT) and dawn (03–09 MLT), as can be seen in Figure 6. Only the R1 current is shown in each sector. The quiet time currents 12 hours before t_0 are slightly larger for MC storms than sheath storms in all sectors. In the hours leading up to storm onset, the FACs during sheath storms increase much faster and reach maximum in all sectors within the first 2 hours after t_0 . During this first hour after t_0 , all sectors in sheath storms have total FACs reaching values larger than 2 MA, with the largest peaks of 2.9 and 3.0 MA seen in the dusk and dawn sectors, respectively. Following the peaks, the FACs in all

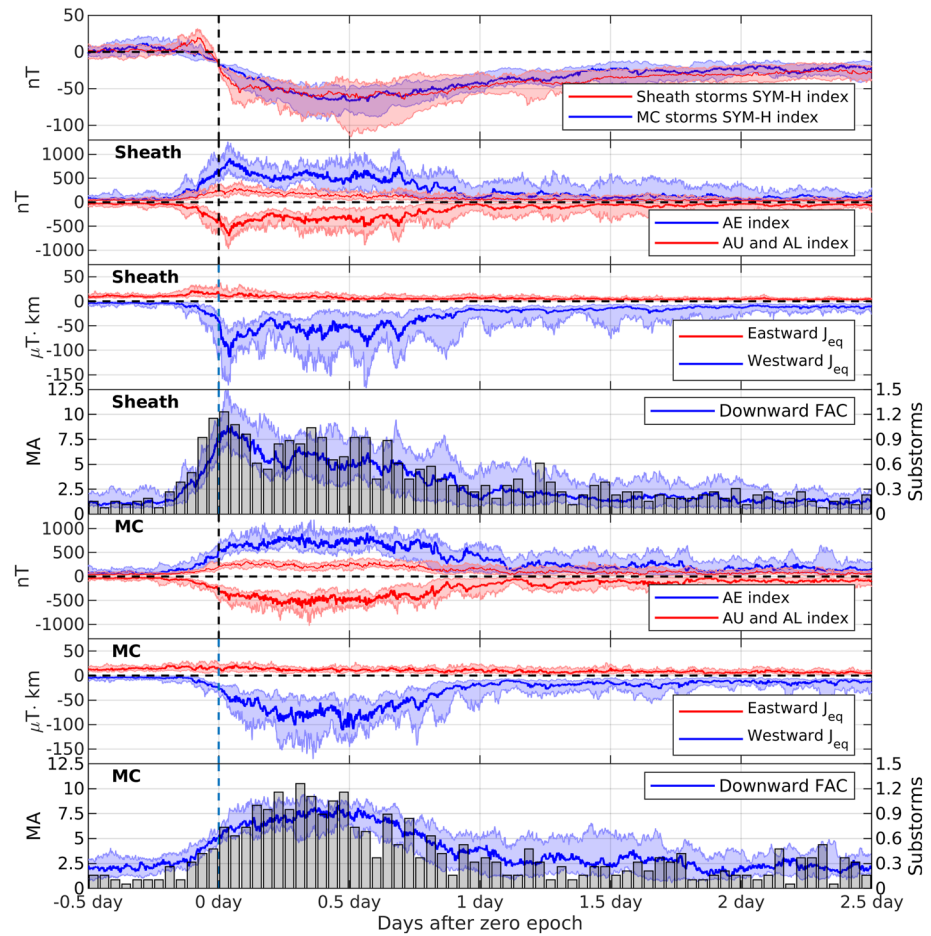


Figure 5. Same as Figure 3, but separated into storms driven by magnetic clouds (MCs) and sheath regions.

sectors decrease during the next 2 hours. After the decrease, the FACs in the noon and midnight sectors remain steady, while smaller maxima are seen in the dusk and dawn sectors 9 and 14 hr after t_0 . Meanwhile, the total FACs in the MC storms show a gradual increase in all sectors. The FACs in the dusk and dawn sectors increase steadily throughout the main phase and become equally large as the FACs in the sheath storms shortly after t_0 . The dusk sector reaches maximum of 3.1 MA 9 hr after t_0 , and the dawn sector reaches maximum of 3.0 MA 13 hr after t_0 . For the noon and midnight sectors, the largest FAC for MC storms do not reach the same strength as for sheath storms. In these sectors the FAC increase during the first 2 hr following t_0 and remain stable in the range of 1.3–1.8 MA throughout the remaining of the storm main phase.

The smaller total currents in the noon and midnight sectors indicate that during the time period when the currents peak, the FACs in sheath storms are more extended into the noon and midnight sectors compared to the FACs in MC storms. The FACs in MC storms reach equally large total currents in the dusk and dawn sectors as sheath storms, but are also more concentrated to these two sectors. This indicates that the interplanetary driver of the two ICME regions and the dynamic pressure play an important role in the spatial extent of the FACs.

Figure 7 shows the superposed FAC and J_{eq} in Altitude Adjusted Corrected Geomagnetic (AACGM) coordinates for the sheath (left) and MC (right) storms at different times with respect to t_0 . A movie showing all times can be found in the Supporting Information S1. Panel a) is at t_0 and shows that the sheath storms have currents that are stronger than in MC storms. This is the case for both the FACs and the J_{eq} . The auroral oval as seen from the FACs is more extended both in longitude and latitude for sheath storms, and the westward electrojet moves more into the evening sector compared with the MC storms. Panel b) shows the currents at the time the total FAC maximizes for the sheath storms. At this time, only slight differences can be seen in the FACs and J_{eq} for the MC storms compared to panel a). However, for the sheath-driven storms the FACs have intensified and expanded,

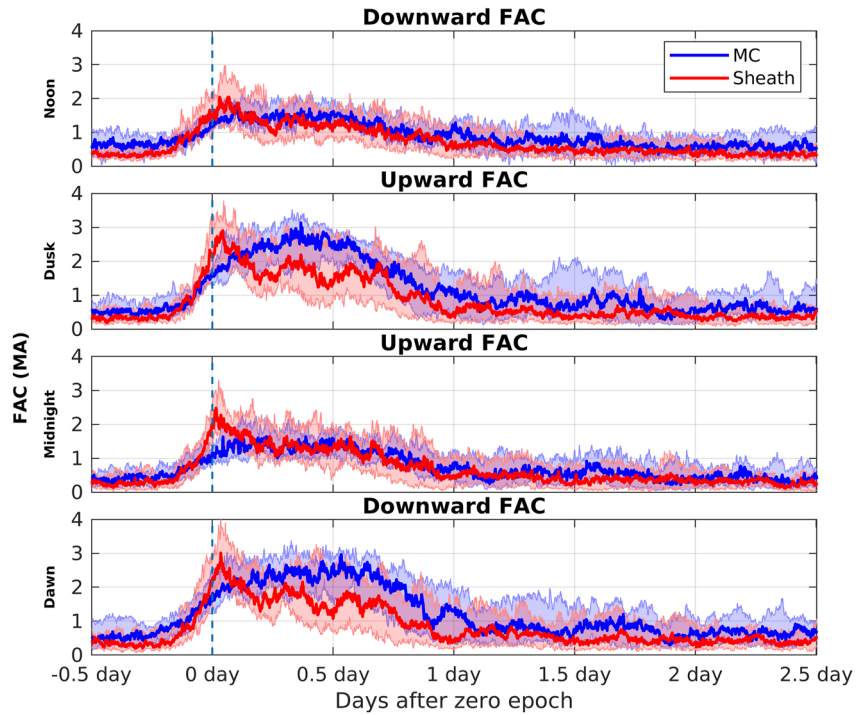


Figure 6. Total field-aligned current (FAC) for magnetic cloud and sheath region driven storms split into four MLT sectors. Only the dominant current orientation (R1) in each sector is shown.

and at this time reach the largest total FAC in the northern hemisphere. The J_{eq} have also grown larger and can be seen enhanced at lower latitudes.

Panel c) is at $t_0 + 11$ hr, at the time the total FAC in the MC storms maximizes. At this time, the majority of the sheath storms are in the storm recovery phase and the currents have diminished to become substantially smaller than seen around t_0 . For the MC storms, both the R1 and R2 FACs in the dusk and dawn sectors have intensified and the westward electrojet has intensified and is extended further into the evening sector compared with the previous panels. Panel d) is at $t_0 + 17$ hr and is in the storm recovery phase in both groups. The currents in sheath storms have further diminished and are close to the quiet time conditions. Meanwhile, the MC storms have also decreased in intensity compared to the storm main phase, but some activity can still be seen in the FACs and electrojets in the dusk and dawn sectors.

4. Discussion

4.1. Russell-McPherron Effect

The varying angle between the Y axis in geocentric solar equatorial coordinates (GSEQ, where IMF is ordered) and the Z axis in geocentric solar magnetospheric coordinates (GSM, where solar wind-magnetosphere coupling is ordered) gives rise to a semi-annual variation in geomagnetic activity known as the Russell-McPherron (RM) effect, which can both affect the strength and prolong the duration of geomagnetic storms (Russell & McPherron, 1973; Zhao & Zong, 2012). Previous studies have shown that the RM effect contributes to a large number of storms occurring around the spring and fall equinoxes (Echer et al., 2011; Russell & McPherron, 1973), and in Paper 1 it was found that 82% of the HSS/SIR driven storms receive a contribution from the RM effect. This section investigates its impact on the ICME storms in this study.

Table 1 column 5 shows the RM effect following the “spring-toward fall-away” (STFA) rule (Miyoshi & Kataoka, 2008) of storms within ± 55 days from the spring or fall equinoxes. According to the STFA rule, around the spring (S) and fall (F) equinoxes, the IMF toward (T) and away (A) polarities have a large projection component in the direction of southward IMF, respectively. Events with contributions from the RM effect (S-T and F-A) are marked in bold text to separate them from events with no contribution (S-A and F-T). Table 1 shows that

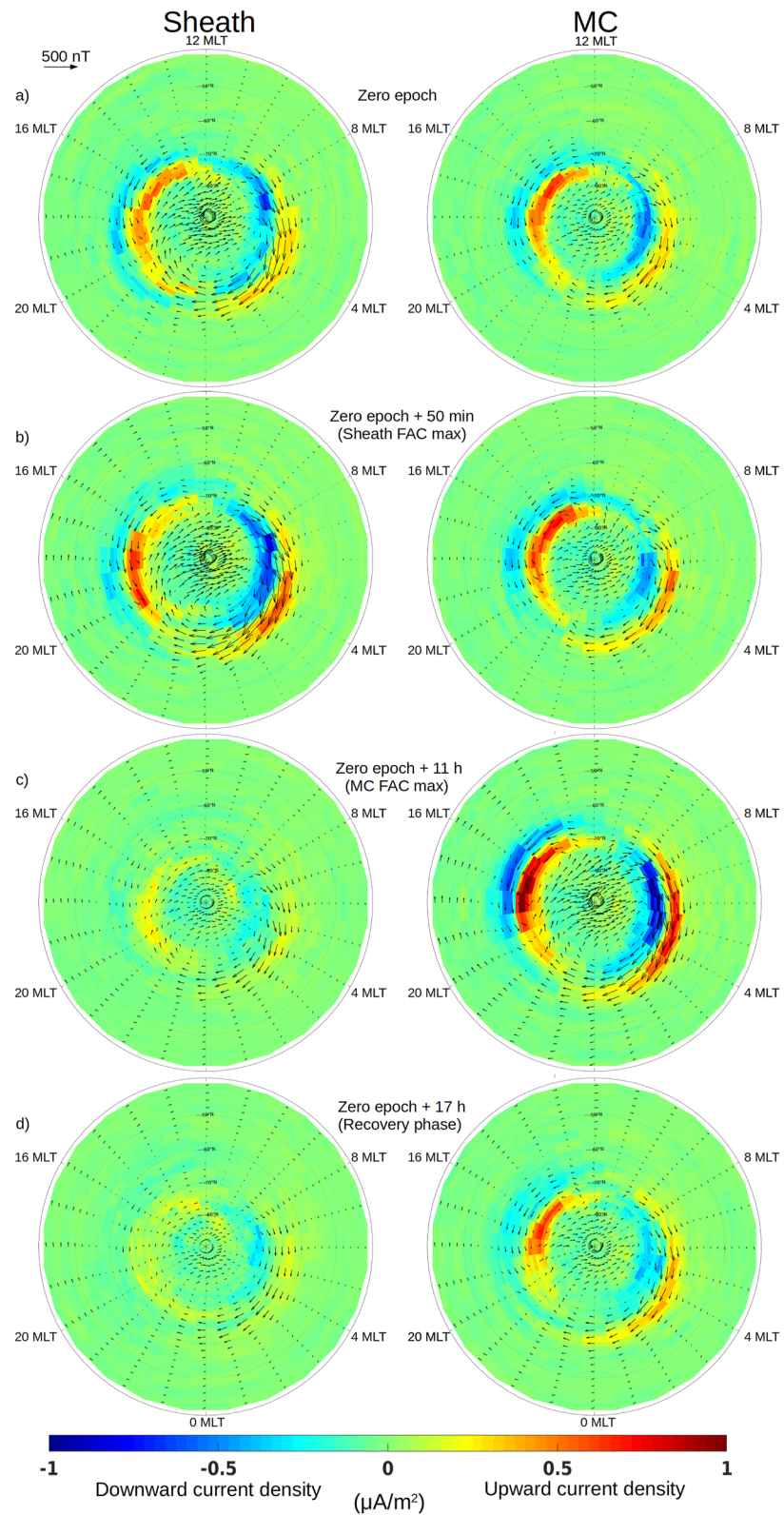


Figure 7. Polar plots of the superposed field-aligned current (FAC) and J_{eq} for sheath (left) and magnetic cloud (MC) (right) storms in Altitude Adjusted Corrected Geomagnetic (AACGM) coordinates at four different times with the respect to the zero epoch.

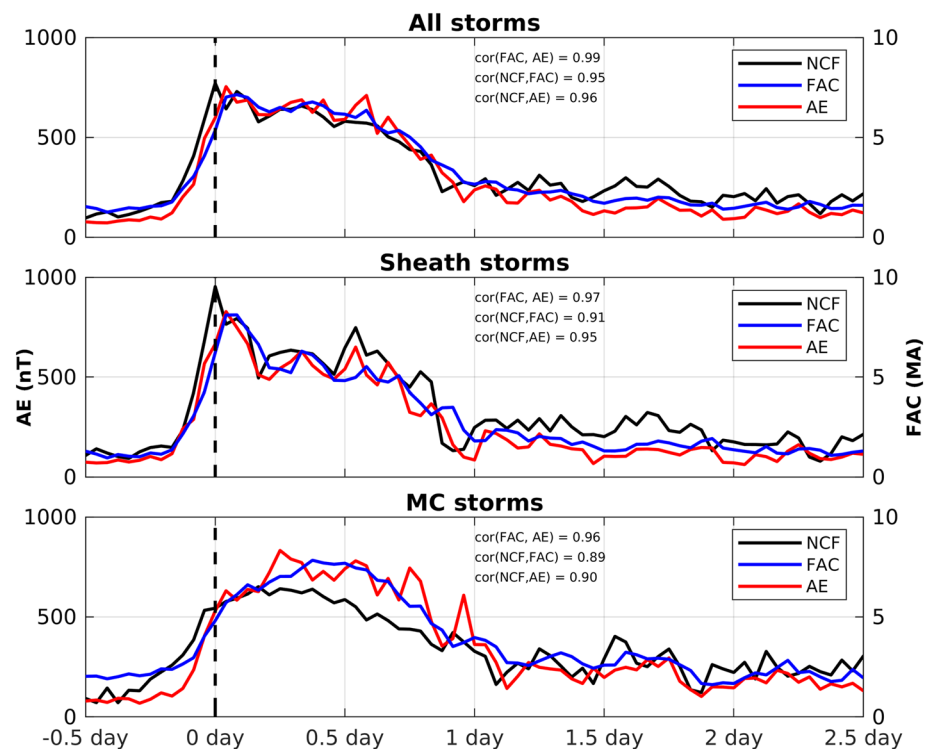


Figure 8. One hour averaged Newell coupling function (NCF), integrated field-aligned current (FAC) and AE index for all, magnetic cloud (MC) and sheath-driven storms. The scale for NCF is 200·AE in all three panels.

20 of the 45 storms (44%) have IMF polarity with a contribution to the southward B_z component from the RM effect. Of these 20 storms, 8 are driven by MCs, while 12 are driven by sheaths. This makes the ratio of storms affected by the RM effect almost equal for both sheath and MC-driven storms, that is 46% and 42% of the storms, respectively.

The fraction of storms that occurred within the equinox intervals in this study was 65%, which is smaller than the value reported in Paper 1 for HSS/SIR storms, where 86% of all storms occurred within the spring and fall equinoxes. Additionally, the fraction of storms with a contribution from the RM effect in this study is 44%, in contrast to 82% in Paper 1. To test the statistical significance of the difference, the Student's t -test was used applying the null hypothesis that the RM effect is equally important in HSS and ICME storms. The test gives p -value 0.004, indicating that the difference is significant with a confidence of 99.6%. This shows that ICME driven storms are less influenced by the RM effect compared with HSS/SIR driven storms.

4.2. SW-Magnetosphere-Ionosphere Coupling

Figure 8 shows the 1 hr averaged superposed Newell coupling function (NCF), integrated FAC and AE index for the three categories: all, sheath and MC-driven storms calculated from 0.5 days before t_0 to 1.5 days after. The Pearson correlation coefficient between the NCF and FAC is 0.95 for all storms and all the three parameters have very high correlations, indicating that the auroral currents are strongly driven by the solar wind coupling as estimated by NCF. The correlation between the AE index and integrated FAC is very high, between 0.96 and 0.99 for the different categories. In Figure 8 there is indication that the NCF precedes the FAC and AE index by about 1 hr (the resolution of data) in the superposed data. It also seems that geoefficiency, as measured by the ratio FAC/NCF or AE/NCF, is different for the sheath and MC-driven storms. Possible reasons for the time delay and the geoefficiency between the solar wind coupling and the currents are topics for a future study.

The correlation coefficients between the NCF and the integrated FAC and AE index are higher than the correlations between Akasofu ϵ and integrated FAC and AE index reported in Paper 1 for the HSS/SIR driven storms. By recalculating the correlation coefficients in Paper 1 using the NCF instead of Akasofu ϵ from 0.5 days before

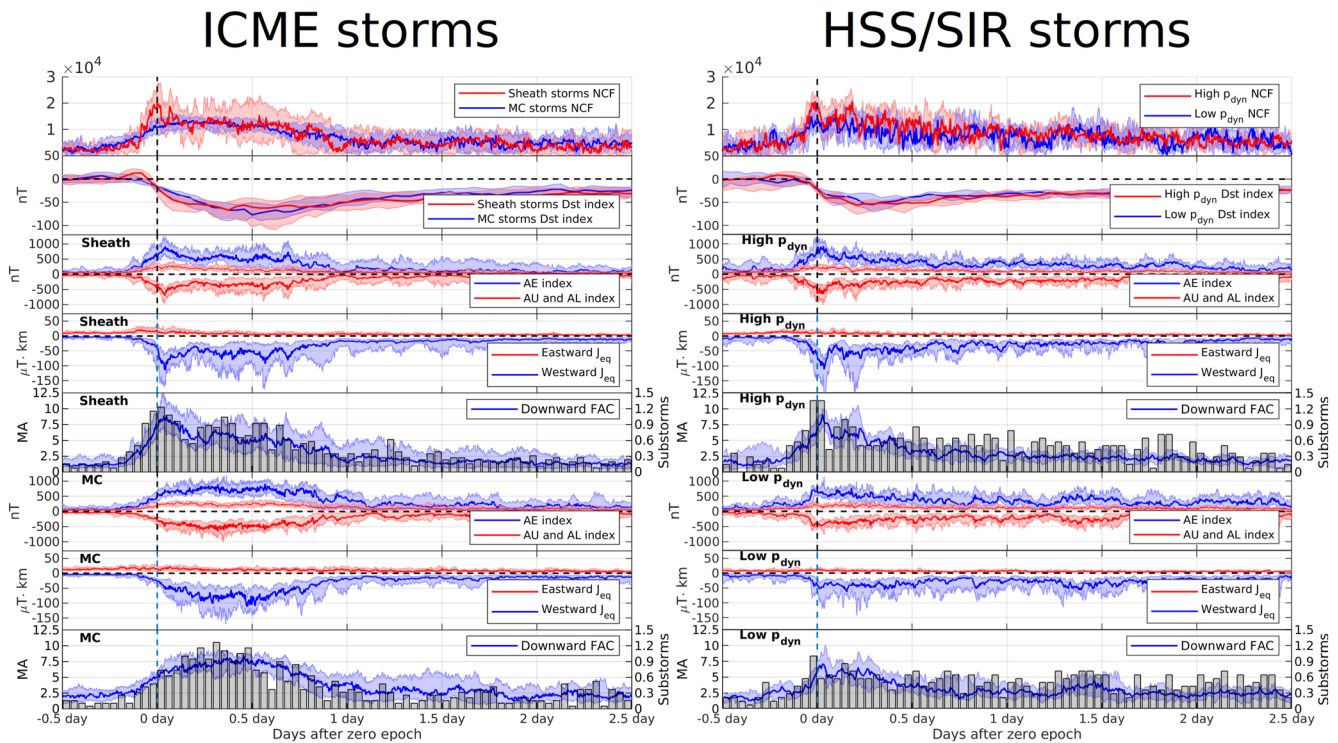


Figure 9. Comparison between interplanetary coronal mass ejection (ICME) driven storms (left) and the high speed streams/stream interaction regions (HSS/SIR) driven storms studied in Paper 1 (right). The two top panels show the Newell coupling function (NCF) and Dst index for both the magnetic cloud (MC) and sheath ICME storms, and the low and high p_{dyn} HSS/SIR storms. Panels 3 through 5 show the AE indices, integrated eastward and westward electrojets and integrated downward field-aligned current (FAC) with the number of substorm onsets for the sheath ICME storms and high p_{dyn} HSS/SIR storms, while panels 6 through 8 show the same parameters for the MC ICME storms and low p_{dyn} HSS/SIR storms.

t_0 to 1.5 days after, the Pearson correlation coefficient between the NCF and FAC is 0.86 and between the NCF and AE index is 0.90, both smaller than for ICME driven storms (0.95 and 0.96, respectively). The correlation between the FAC and AE index was also smaller in Paper 1 compared to this study.

It should be noted that for individual events, the correlation coefficients are smaller than with the superposed data shown in Figure 8. From all the individual storms the median correlation coefficient between the AE index and integrated FAC is 0.84, NCF and integrated FAC 0.78, and NCF and AE index 0.77. This shows that the correlations from the statistical superposed data are larger than for individual events, likely because SEA smooths some of the fluctuations.

4.3. ICME Versus HSS/SIR-Driven Storms

Figure 9 shows a comparison of the ICME driven storms and HSS/SIR driven storms from Paper 1. The top panels show the NCF for the sheath and MC ICME storms and the high and low p_{dyn} HSS/SIR storms. For both the sheath ICME and high p_{dyn} HSS/SIR, the NCF peaks about 1 hr before t_0 , followed by a second maximum several hours after t_0 (later for HSS/SIR than ICME). The NCF in the MC and low p_{dyn} HSS/SIR storms are smaller than in the sheath and high p_{dyn} HSS/SIR storms during the storm main and early recovery phases and the duration of elevated NCF after main phase onset is longer for ICME than HSS/SIR storms. In the second panels the Dst indices are shown. Only the sheath and high p_{dyn} HSS/SIR storms show signatures of SSCs with a positive excursion in the Dst index before t_0 . The sheath storms have a larger excursion than the high p_{dyn} HSS/SIR storms, indicating larger magnetopause currents due to compression. The difference between the development in the Dst index between the sheath and MC storms is larger than between the high and low p_{dyn} HSS/SIR storms. The sheath storms have the steepest decrease in the Dst index at the time of main phase onset, while the MC storms have the slowest decrease and also longer main phase duration than sheath storms (12 and 9 hr, respectively).

Table 3

Summary of Selected Properties of the Superposed Sheath and MC ICME Storms, and the Superposed High and Low p_{dyn} HSS/SIR Storms From Paper 1

	ICME		HSS/SIR	
	Sheath	MC	High	Low
Max NCF (10^3)	20.2	13.5	20.6	15.0
Max total westward J_{eq} ($\mu\text{T}\cdot\text{km}$)	114	112	111	64
Max integrated downward FAC (MA)	8.9	8.4	9.2	7.1
Time of max integrated FAC (after t_0)	50 min	11.0 hr	40 min	40 min
Total downward FAC [t_0 , $t_0 + 12$ hr] (MAh)	73.3	82.8	68.9	64.5
Total downward FAC [$t_0 + 48$ hr, $t_0 + 60$ hr] (MAh)	15.6	26.3	21.0	29.6
Number of substorm onsets [t_0 , $t_0 + 12$ hr]	11.2	12.4	9.3	7.8
Number of substorm onsets [$t_0 + 48$ hr, $t_0 + 60$ hr]	2.3	3.1	3.3	6.4
Max Dst [$t_0 - 12$ hr, t_0] (nT)	13	7	9	2
Storms affected by Russell-McPherron effect	46%	42%	79%	86%

Note. FAC, field-aligned current; HSS/SIR, high speed streams stream interaction regions; ICME, interplanetary coronal mass ejection; MC, magnetic cloud; NCF, Newell coupling function.

Additionally, HSS/SIR storms have shorter main phase durations than the ICME storms, with the high p_{dyn} HSS/SIR storms being slightly shorter than the low p_{dyn} HSS/SIR storms (5 and 7 hr, respectively).

Panels 3 through 5 from the top for ICME and HSS/SIR storms in Figure 9 show the AE indices, integrated eastward and westward equivalent currents and the integrated downward FAC with the number of substorm onsets for the sheath (high p_{dyn}) ICME storms and high p_{dyn} HSS/SIR storms. Several similarities can be observed in the currents of sheath and high p_{dyn} HSS/SIR storms. First, the currents and number of substorm onsets peak within 1 hr after storm onset. Second, there are two clear peaks in the integrated westward electrojet, integrated FAC and number of substorm onsets, one near storm onset and the latter several hours later near the end of the storm main phase. The maximum integrated FACs have about similar strengths in the sheath and high p_{dyn} HSS/SIR storms (8.9 and 9.2 MA, respectively), but the sheath storms have a longer duration of large currents during the storm main and early recovery phase. In the late recovery phase, from 1 day after t_0 , this situation reverses and the high p_{dyn} HSS/SIR storms have more substorm onsets and larger currents than the sheath storms.

Panels 6 through 8 from the top for ICME and HSS/SIR storms show the same parameters for the MC (low p_{dyn}) ICME storms and low p_{dyn} HSS/SIR storms. The MC storms have currents and number of substorm onsets that reach maxima around the time of Dst minimum, with integrated FAC peaking at 8.4 MA. For the low p_{dyn} HSS/SIR storms, the currents and number of substorm onsets have high values during the Dst minimum, too, but the peak integrated FAC occurs 1 hr after onset and is of lower strength, only 7.1 MA. The number of substorm onsets also peaks later for MC storms compared to the low p_{dyn} HSS/SIR storms, with both categories having the largest numbers around the time of peak currents. The peak currents, as well as the total time-integrated current and number of substorm onsets are all larger for MC storms than for the low p_{dyn} HSS/SIR storms during the storm main and early recovery phase. As in the sheath and high p_{dyn} HSS/SIR storms, this situation reverses in the late recovery phase, where more activity is seen in the low p_{dyn} HSS/SIR storms than in the MC storms. This shows that the HSS/SIR storms drive the ionospheric current systems longer than ICMEs do, although the ICME storms drive larger FACs and ionospheric currents during the storm main and early recovery phase.

Table 3 summarizes quantitatively some selected properties of the ICME and HSS/SIR storms. The largest values of the NCF, integrated westward J_{eq} and integrated FAC are seen in the sheath and high p_{dyn} HSS/SIR storms. The time of maximum integrated FAC occurs sooner after t_0 for the sheath (50 min) and HSS/SIR (40 min) storms than for the MC storms (11 hr). Further, the total FAC and number of substorm onsets within the first 12 hr after t_0 are higher for ICME storms than HSS/SIR storms. Within the ICME storms, the MC storms have larger total time-integrated current and number of substorm onsets than the sheath storms. Within the HSS/SIR storms the high p_{dyn} storms have more current and substorms than the low p_{dyn} storms. This situation changes in the late recovery phase, as the total FAC and number of substorm onsets between [$t_0 + 48$ hr, $t_0 + 60$ hr] is highest for the

low p_{dyn} HSS/SIR storms. The most pronounced SSCs in terms of Dst enhancement before the main phase onset are in the sheath and high p_{dyn} storms. A minor enhancement in the Dst index can be seen for the MC storms 7 hr before t_0 , while no enhancement was seen for the low p_{dyn} HSS/SIR. The bottom line shows that the fraction of storms affected by the RM effect is much lower for ICME storms than HSS/SIR storms.

Overall, Table 3 shows greater similarity between the currents in sheath and high p_{dyn} HSS/SIR storms, than between the currents in sheath and MC storms. This can be explained by the fact that both low and high p_{dyn} HSS/SIR storms are mainly driven by the SIR ahead of the HSS, as was shown in Paper 1. The stream interface comprising the SIR contains solar wind with some similar properties as the sheath region, that is, compressed solar wind plasma and fluctuating magnetic field.

5. Conclusions

This study analyzes and reports the ionospheric equivalent currents and FACs, as well as the driving parameters of the solar wind and IMF during ICME driven storms for which the minimum Dst index is below -50 nT. The statistical behavior of the currents, solar wind and IMF were extracted using a superposed epoch analysis with zero epoch (t_0) set to the onset of the storm main phase (when the 10 min averaged SYM-H index decreased below -15 nT). The storms were also separated into low and high dynamic pressure groups based on the maximum solar wind dynamic pressure in the ± 3 hr interval around t_0 , as was done in Pedersen et al. (2021) for HSS/SIR driven storms, referred to as Paper 1. It is found that high p_{dyn} storms are driven by the sheath region ahead of the ICME ejecta and low p_{dyn} storms are driven by the MC structure of the ICME. The FACs and ionospheric equivalent currents resulting from the sheath and MC storms are analyzed and compared with the results reported in Paper 1. This is, to our knowledge, the first superposed epoch study reporting the statistical behavior of the global FACs and equivalent ionospheric currents during moderate-to-large ICME sheath and MC-driven geomagnetic storms.

The main findings of this study are the following:

- For all ICME storms, the superposed SYM-H minimum is -64 nT and is reached 9 hr after t_0 . This makes the main phase of ICME storms typically of larger magnitude and of longer duration compared with the HSS/SIR storms studied in Paper 1 where the corresponding values were -54 nT and 6 hr. This is in agreement with earlier studies that ICMEs drive larger storms with typically longer main phase durations than HSSs/SIRs (e.g., Borovsky & Denton, 2006; Yermolaev et al., 2014).
- For all ICME storms, the integrated FAC maximizes about 1 hr after t_0 with the superposed upward and downward FACs being 7.7 MA each. The integrated westward J_{eq} , AE index and number of substorm onsets also peak within the first hour after t_0 , and have high values throughout the entire storm main phase until $t_0 + 13$ hr.
- Sheath-driven (high p_{dyn}) storms develop rapidly and have FACs that peak 50 min after t_0 with values of 8.9 MA, while the MC-driven (low p_{dyn}) storms develop gradually and have FACs that peak 11 hr after t_0 at 8.4 MA. The response in the currents found in this study is in line with previous studies showing that the magnetosphere and auroral activity have a faster response at storm onset in sheath storms compared with MC storms (Huttunen et al., 2002; Pulkkinen et al., 2007).
- Durations of storm main phases are 9 hr for sheath-driven storms and 12 hr for MC-driven storms. During the first 4 hr after storm onset, sheath-driven storms have typically larger FAC and ionospheric currents than MC-driven storms. Toward the SYM-H minimum and in the recovery phase the currents and number of substorm onsets in the MC-driven storms are substantially larger than in the sheath-driven storms.
- The results show that the Russell-McPherron effect is more important in HSS/SIR driven storms compared to ICME driven storms. Twenty of 45 ICME storms (44%) receive a contribution from the Russell-McPherron effect, which is significantly less than the 82% for the HSS/SIR driven storms reported in Paper 1.
- The Pearson correlation coefficients between the 1-hr averaged superposed Newell coupling function and integrated FAC is found to be 0.95 for all storms, indicating that ICME storms are strongly driven by the solar wind.
- During the first 12 hr after main phase onset, the total FAC and number of substorms in sheath and MC-driven storms are larger than in HSS/SIR driven storms.
- After 2 days from main phase onset, the total FAC and number of substorms are larger for HSS/SIR driven storms than ICME driven storms. This shows that the longer lasting impact of HSS/SIR storms compared

with ICME storms (e.g., Borovsky & Denton, 2006; Burns et al., 2012; Turner et al., 2009) also extends to the FACs and ionospheric currents.

Data Availability Statement

All data used in this study can be freely accessed through the links given in the acknowledgements.

Acknowledgments

This work was supported by the Academy of Finland project 314664 and 314670. We thank the AMPERE team and the AMPERE Science Center for providing the Iridium derived data products (<https://ampere.jhuapl.edu/>). For the ground magnetometer data and substorm onset list, we gratefully thank the SuperMAG collaboration and all organizations involved (<https://supermag.jhuapl.edu/info/>). For the geomagnetic indices, solar wind and interplanetary magnetic field data, we gratefully thank NASA/GSFC's Space Physics Data Facility's OMNIWeb (<https://omniweb.gsfc.nasa.gov/>).

References

- Alves, M., Echer, E., & Gonzalez, W. (2006). Geoeffectiveness of corotating interaction regions as measured by Dst index. *Journal of Geophysical Research*, 111(A7), A07S05. <https://doi.org/10.1029/2005JA011379>
- Anderson, B., Takahashi, K., Kamei, T., Waters, C., & Toth, B. (2002). Birkeland current system key parameters derived from iridium observations: Method and initial validation results. *Journal of Geophysical Research*, 107(A6), 1079. <https://doi.org/10.1029/2001JA000080>
- Anderson, B., Takahashi, K., & Toth, B. A. (2000). Sensing global birkeland currents with iridium® engineering magnetometer data. *Geophysical Research Letters*, 27(24), 4045–4048. <https://doi.org/10.1029/2000GL000094>
- Borovsky, J. E., & Denton, M. H. (2006). Differences between CME-driven storms and CIR-driven storms. *Journal of Geophysical Research*, 111(A7), A07S08. <https://doi.org/10.1029/2005JA011447>
- Boudouridis, A., Zesta, E., Lyons, L., Anderson, P., & Lummerzheim, D. (2005). Enhanced solar wind geoeffectiveness after a sudden increase in dynamic pressure during southward IMF orientation. *Journal of Geophysical Research*, 110(A5), A05214. <https://doi.org/10.1029/2004JA010704>
- Burlaga, L., Klein, L., Sheeley, N., Jr., Michels, D., Howard, R., Koomen, M., et al. (1982). A magnetic cloud and a coronal mass ejection. *Geophysical Research Letters*, 9(12), 1317–1320. <https://doi.org/10.1029/GL009i012p01317>
- Burlaga, L., Sittler, E., Mariani, F., & Schwenn, A. R. (1981). Magnetic loop behind an interplanetary shock: Voyager, Helios, and IMP 8 observations. *Journal of Geophysical Research*, 86(A8), 6673–6684. <https://doi.org/10.1029/JA086iA08p06673>
- Burns, A., Solomon, S., Qian, L., Wang, W., Emery, B., Wiltberger, M., & Weimer, D. (2012). The effects of corotating interaction region/high speed stream storms on the thermosphere and ionosphere during the last solar minimum. *Journal of Atmospheric and Solar-Terrestrial Physics*, 83, 79–87. <https://doi.org/10.1016/j.jastp.2012.02.006>
- Cane, H., & Richardson, I. (2003). Interplanetary coronal mass ejections in the near-earth solar wind during 1996–2002. *Journal of Geophysical Research*, 108(A4), 1156. <https://doi.org/10.1029/2002ja009817>
- Clausen, L. B., Baker, J., Ruohoniemi, J. M., Milan, S. E., Coxon, J., Wing, S., et al. (2013). Temporal and spatial dynamics of the regions 1 and 2 birkeland currents during substorms. *Journal of Geophysical Research: Space Physics*, 118(6), 3007–3016. <https://doi.org/10.1002/jgra.50288>
- Coxon, J., Milan, S. E., Clausen, L., Anderson, B., & Korth, H. (2014). A superposed epoch analysis of the regions 1 and 2 birkeland currents observed by ampere during substorms. *Journal of Geophysical Research: Space Physics*, 119(12), 9834–9846. <https://doi.org/10.1002/2014JA020500>
- Echer, E., Gonzalez, W., & Tsurutani, B. (2011). Statistical studies of geomagnetic storms with peak Dst ≤ - 50 nt from 1957 to 2008. *Journal of Atmospheric and Solar-Terrestrial Physics*, 73(11–12), 1454–1459. <https://doi.org/10.1016/j.jastp.2011.04.021>
- Feldstein, Y. I., Grafe, A., Gromova, L., & Popov, V. (1997). Auroral electrojets during geomagnetic storms. *Journal of Geophysical Research*, 102(A7), 14223–14235. <https://doi.org/10.1029/97JA00577>
- Forsyth, C., Shortt, M., Coxon, J., Rae, I., Freeman, M., Kalmoni, N., et al. (2018). Seasonal and temporal variations of field-aligned currents and ground magnetic deflections during substorms. *Journal of Geophysical Research: Space Physics*, 123(4), 2696–2713. <https://doi.org/10.1002/2017JA025136>
- Gjerloev, J. (2009). A global ground-based magnetometer initiative. *Eos, Transactions American Geophysical Union*, 90(27), 230–231. <https://doi.org/10.1029/2009EO270002>
- Gjerloev, J. (2012). The SuperMAG data processing technique. *Journal of Geophysical Research*, 117(A9), A09213. <https://doi.org/10.1029/2012JA017683>
- Gonzalez, W. D., Joselyn, J. A., Kamide, Y., Kroehl, H. W., Rostoker, G., Tsurutani, B. T., & Vasyliunas, V. M. (1994). What is a geomagnetic storm? *Journal of Geophysical Research*, 99(A4), 5771–5792. <https://doi.org/10.1029/93JA02867>
- Gosling, J. (1990). Coronal mass ejections and magnetic flux ropes in interplanetary space. *Physics of Magnetic Flux Ropes*, 58, 343–364. <https://doi.org/10.1029/GM058p0343>
- Gosling, J., Asbridge, J., Bame, S., & Feldman, W. (1978). Solar wind stream interfaces. *Journal of Geophysical Research*, 83(A4), 1401–1412. <https://doi.org/10.1029/JA083iA04p01401>
- Gosling, J., Pizzo, V., & Bame, S. J. (1973). Anomalous low proton temperatures in the solar wind following interplanetary shock waves—Evidence for magnetic bottles? *Journal of Geophysical Research*, 78(13), 2001–2009. <https://doi.org/10.1029/JA078i013p02001>
- Grandin, M., Aikio, A. T., & Kozlovsky, A. (2019). Properties and geoeffectiveness of solar wind high-speed streams and stream interaction regions during solar cycles 23 and 24. *Journal of Geophysical Research: Space Physics*, 124(6), 3871–3892. <https://doi.org/10.1029/2018JA026396>
- Hutchinson, J. A., Wright, D., & Milan, S. (2011). Geomagnetic storms over the last solar cycle: A superposed epoch analysis. *Journal of Geophysical Research*, 116(A9), A09211. <https://doi.org/10.1029/2011JA016463>
- Huttunen, K. E. J., Koskinen, H. E., & Schwenn, R. (2002). Variability of magnetospheric storms driven by different solar wind perturbations. *Journal of Geophysical Research*, 107(A7), 1121. <https://doi.org/10.1029/2001JA900171>
- Iijima, T., & Potemra, T. A. (1978). Large-scale characteristics of field-aligned currents associated with substorms. *Journal of Geophysical Research*, 83(A2), 599–615. <https://doi.org/10.1029/JA083iA02p00599>
- Ilie, R., Liemohn, M. W., Thomsen, M. F., Borovsky, J. E., & Zhang, J. (2008). Influence of epoch time selection on the results of superposed epoch analysis using ACE and MPA data. *Journal of Geophysical Research*, 113(A3), A00A14. <https://doi.org/10.1029/2008JA013241>
- Jian, L., Russell, C., Luhmann, J., & Skoug, R. (2006). Properties of interplanetary coronal mass ejections at one au during 1995–2004. *Solar Physics*, 239(1), 393–436. <https://doi.org/10.1007/s11207-006-0133-2>
- Käki, S., Viljanen, A., Juusola, L., & Kauristie, K. (2022). Spatio-temporal development of large-scale auroral electrojet currents relative to substorm onsets. *Annales Geophysicae*, 40(1), 107–119. <https://doi.org/10.5194/angeo-40-107-2022>
- Kamide, Y., Baumjohann, W., Daglis, I. A., Gonzalez, W. D., Grande, M., Joselyn, J. A., et al. (1998). Current understanding of magnetic storms: Storm-substorm relationships. *Journal of Geophysical Research*, 103(A8), 17705–17728. <https://doi.org/10.1029/98JA01426>

- Kilpua, E., Koskinen, H. E., & Pulkkinen, T. I. (2017). Coronal mass ejections and their sheath regions in interplanetary space. *Living Reviews in Solar Physics*, *14*(1), 1–83. <https://doi.org/10.1007/s41116-017-0009-6>
- King, J., & Papitashvili, N. (2005). Solar wind spatial scales in and comparisons of hourly wind and ace plasma and magnetic field data. *Journal of Geophysical Research*, *110*(A2), A02104. <https://doi.org/10.1029/2004JA010649>
- Klein, L., & Burlaga, L. (1982). Interplanetary magnetic clouds at 1 Au. *Journal of Geophysical Research*, *87*(A2), 613–624. <https://doi.org/10.1029/JA087iA02p00613>
- Knipp, D., Matsuo, T., Kilcommons, L., Richmond, A., Anderson, B., Korth, H., et al. (2014). Comparison of magnetic perturbation data from LEO satellite constellations: Statistics of DMSP and AMPERE. *Space Weather*, *12*(1), 2–23. <https://doi.org/10.1002/2013SW000987>
- Le, G., Lühr, H., Anderson, B., Strangeway, R., Russell, C., Singer, H., et al. (2016). Magnetopause erosion during the 17 march 2015 magnetic storm: Combined field-aligned currents, auroral oval, and magnetopause observations. *Geophysical Research Letters*, *43*(6), 2396–2404. <https://doi.org/10.1002/2016GL068257>
- Lepping, R., Berdichevsky, D., Szabo, A., Arqueros, C., & Lazarus, A. (2003). Profile of an average magnetic cloud at 1 au for the quiet solar phase: Wind observations. *Solar Physics*, *212*(2), 425–444. <https://doi.org/10.1023/A:1022938903870>
- Loewe, C., & Pröls, G. (1997). Classification and mean behavior of magnetic storms. *Journal of Geophysical Research*, *102*(A7), 14209–14213. <https://doi.org/10.1029/96JA04020>
- Lyons, L., Gallardo-Lacourt, B., Zou, S., Weygand, J., Nishimura, Y., Li, W., et al. (2016). The 17 march 2013 storm: Synergy of observations related to electric field modes and their ionospheric and magnetospheric effects. *Journal of Geophysical Research: Space Physics*, *121*(11), 10–880. <https://doi.org/10.1002/2016JA023237>
- McPherron, R. (1979). Magnetospheric substorms. *Reviews of Geophysics*, *17*(4), 657–681. <https://doi.org/10.1029/RG017i004p00657>
- McPherron, R., Anderson, B., & Chu, X. (2018). Relation of field-aligned currents measured by the network of iridium@ spacecraft to solar wind and substorms. *Geophysical Research Letters*, *45*(5), 2151–2158. <https://doi.org/10.1002/2017GL076741>
- Miyoshi, Y., & Kataoka, R. (2008). Flux enhancement of the outer radiation belt electrons after the arrival of stream interaction regions. *Journal of Geophysical Research*, *113*(A3), A03S09. <https://doi.org/10.1029/2007JA012506>
- Nakano, S., & Kataoka, R. (2022). Echo state network model for analyzing solar-wind effects on the Au and Al indices. *Annales Geophysicae*, *40*(1), 11–22. <https://doi.org/10.5194/angeo-40-11-2022>
- Newell, P., & Gjerloev, J. (2011a). Evaluation of SuperMAG auroral electrojet indices as indicators of substorms and auroral power. *Journal of Geophysical Research*, *116*(A12), A12211. <https://doi.org/10.1029/2011JA016779>
- Newell, P., & Gjerloev, J. (2011b). Substorm and magnetosphere characteristic scales inferred from the supermag auroral electrojet indices. *Journal of Geophysical Research*, *116*(A12), A12232. <https://doi.org/10.1029/2011JA016936>
- Newell, P., Sotirelis, T., Liou, K., Meng, C.-I., & Rich, F. (2007). A nearly universal solar wind-magnetosphere coupling function inferred from 10 magnetospheric state variables. *Journal of Geophysical Research*, *112*(A1), A01206. <https://doi.org/10.1029/2006JA012015>
- Palmroth, M., Pulkkinen, T., Janhunen, P., McComas, D., Smith, C., & Koskinen, H. (2004). Role of solar wind dynamic pressure in driving ionospheric joule heating. *Journal of Geophysical Research*, *109*(A11), A11302. <https://doi.org/10.1029/2004JA010529>
- Pedersen, M. N., Vanhamäki, H., Aikio, A. T., Käki, S., Workayehu, A. B., Waters, C. L., & Gjerloev, J. W. (2021). Field-aligned and ionospheric currents by ampere and SuperMAG during HSS/SIR-driven storms. *Journal of Geophysical Research: Space Physics*, *126*(11), e2021JA029437. <https://doi.org/10.1029/2021JA029437>
- Pulkkinen, T. I., Partamies, N., Huttunen, K., Reeves, G., & Koskinen, H. (2007). Differences in geomagnetic storms driven by magnetic clouds and ICME sheath regions. *Geophysical Research Letters*, *34*(2), L02105. <https://doi.org/10.1029/2006GL027775>
- Richardson, I., & Cane, H. V. (2010). Near-earth interplanetary coronal mass ejections during solar cycle 23 (1996–2009): Catalog and summary of properties. *Solar Physics*, *264*(1), 189–237. <https://doi.org/10.1007/s11207-010-9568-6>
- Richardson, I., Cliver, E., & Cane, H. (2001). Sources of geomagnetic storms for solar minimum and maximum conditions during 1972–2000. *Geophysical Research Letters*, *28*(13), 2569–2572. <https://doi.org/10.1029/2001GL013052>
- Russell, C., & McPherron, R. (1973). Semiannual variation of geomagnetic activity. *Journal of Geophysical Research*, *78*(1), 92–108. <https://doi.org/10.1029/JA078i001p00092>
- Siscoe, G., & Odstroil, D. (2008). Ways in which ICME sheaths differ from magnetosheaths. *Journal of Geophysical Research*, *113*(A9), A00B07. <https://doi.org/10.1029/2008JA013142>
- Smith, E., Slavin, J., Zwickl, R., & Bame, S. (1986). Shocks and storm sudden commencements. *Solar Wind Magnetosphere Coupling*, *126*, 345. https://doi.org/10.1007/978-90-277-2303-1_25
- Turner, N. E., Cramer, W. D., Earles, S. K., & Emery, B. A. (2009). Geoefficiency and energy partitioning in CIR-driven and CME-driven storms. *Journal of Atmospheric and Solar-Terrestrial Physics*, *71*(10–11), 1023–1031. <https://doi.org/10.1016/j.jastp.2009.02.005>
- Vourlidis, A., Lynch, B. J., Howard, R. A., & Li, Y. (2013). How many CMEs have flux ropes? Deciphering the signatures of shocks, flux ropes, and prominences in coronagraph observations of CMEs. *Solar Physics*, *284*(1), 179–201. <https://doi.org/10.1007/s11207-012-0084-8>
- Wang, C., Li, C., Huang, Z., & Richardson, J. (2006). Effect of interplanetary shock strengths and orientations on storm sudden commencement rise times. *Geophysical Research Letters*, *33*(14), L14104. <https://doi.org/10.1029/2006GL025966>
- Wanliss, J. A., & Showalter, K. M. (2006). High-resolution global storm index: Dst versus SYM-H. *Journal of Geophysical Research*, *111*(A2), A02202. <https://doi.org/10.1029/2005JA011034>
- Waters, C., Anderson, B., Green, D. L., Korth, H., Barnes, R. J., & Vanhamäki, H. (2020). Science data products for ampere. In M. W. Dunlop & H. Lühr (Eds.), *Ionospheric multi-spacecraft analysis tools: Approaches for deriving ionospheric parameters* (pp. 141–165). Springer International Publishing. https://doi.org/10.1007/978-3-030-26732-2_7
- Waters, C., Anderson, B., & Liou, K. (2001). Estimation of global field aligned currents using the iridium@ system magnetometer data. *Geophysical Research Letters*, *28*(11), 2165–2168. <https://doi.org/10.1029/2000GL012725>
- Waters, C., Gjerloev, J., Dupont, M., & Barnes, R. (2015). Global maps of ground magnetometer data. *Journal of Geophysical Research: Space Physics*, *120*(11), 9651–9660. <https://doi.org/10.1002/2015JA021596>
- Wilder, F., Crowley, G., Anderson, B., & Richmond, A. (2012). Intense dayside joule heating during the 5 April 2010 geomagnetic storm recovery phase observed by AMIE and AMPERE. *Journal of Geophysical Research*, *117*(A5), A05207. <https://doi.org/10.1029/2011JA017262>
- Yermolaev, Y. I., Lodkina, I. G., Dremukhina, L. A., Yermolaev, M. Y., & Khokhlachev, A. A. (2021). What solar–terrestrial link researchers should know about interplanetary drivers. *Universe*, *7*(5), 138. <https://doi.org/10.3390/universe7050138>
- Yermolaev, Y. I., Lodkina, I. G., Nikolaeva, N., & Yermolaev, M. Y. (2014). Influence of the interplanetary driver type on the durations of the main and recovery phases of magnetic storms. *Journal of Geophysical Research: Space Physics*, *119*(10), 8126–8136. <https://doi.org/10.1002/2014JA019826>

- Yermolaev, Y. I., Nikolaeva, N., Lodkina, I. G., & Yermolaev, M. Y. (2010). Specific interplanetary conditions for CIR-sheath-and ICME-induced geomagnetic storms obtained by double superposed epoch analysis. *Annales Geophysicae*, 28(12), 2177–2186. <https://doi.org/10.5194/angeo-28-2177-2010>
- Yermolaev, Y. I., Nikolaeva, N., Lodkina, I. G., & Yermolaev, M. Y. (2012). Geoeffectiveness and efficiency of CIR, sheath, and ICME in generation of magnetic storms. *Journal of Geophysical Research*, 117(A9), A00L07. <https://doi.org/10.1029/2011JA017139>
- Yermolaev, Y. I., Yermolaev, M. Y., Lodkina, I. G., & Nikolaeva, N. (2007). Statistical investigation of heliospheric conditions resulting in magnetic storms. *Cosmic Research*, 45(1), 1–8. <https://doi.org/10.1134/S0010952507010017>
- Yokoyama, N., & Kamide, Y. (1997). Statistical nature of geomagnetic storms. *Journal of Geophysical Research*, 102(A7), 14215–14222. <https://doi.org/10.1029/97JA00903>
- Zhao, H., & Zong, Q.-G. (2012). Seasonal and diurnal variation of geomagnetic activity: Russell-McPherron effect during different IMF polarity and/or extreme solar wind conditions. *Journal of Geophysical Research*, 117(A11), A11222. <https://doi.org/10.1029/2012JA017845>